ADVANCED ENERGY MATERIALS

www.advenergymat.de

A High Voltage Aqueous Zinc–Organic Hybrid Flow Battery

Minjoon Park, Eugene S. Beh, Eric M. Fell, Yan Jing, Emily F. Kerr, Diana De Porcellinis, Marc-Antoni Goulet, Jaechan Ryu, Andrew A. Wong, Roy G. Gordon, Jaephil Cho, and Michael J. Aziz**

Water-soluble redox-active organic molecules have attracted extensive attention as electrical energy storage alternatives to redox-active metals that are low in abundance and high in cost. Here an aqueous zinc–organic hybrid redox flow battery (RFB) is reported with a positive electrolyte comprising a functionalized 1,4-hydroquinone bearing four (dimethylamino)methyl groups dissolved in sulfuric acid. By utilizing a three-electrolyte, two-membrane configuration this acidic positive electrolyte is effectively paired with an alkaline negative electrolyte comprising a $Zn/[Zn(OH)_4]^{2-}$ redox couple and a hybrid RFB is operated at a high operating voltage of 2.0 V. It is shown that the electrochemical reversibility and kinetics of the organic redox species can be enhanced by an electrocatalyst, leading to a cyclic voltammetry peak separation as low as 35 mV and enabling an enhanced rate capability.

1. Introduction

Redox flow batteries (RFBs) are among the most promising large-scale energy storage systems for the regulation of the intermittency and variability of power from renewable energy sources such as solar and wind.[1,2] True RFBs store the electrical energy in external reservoirs of solution-state active materials in which all oxidation states are soluble. In contrast, hybrid RFBs electrodeposit at least one active species, e.g., lithium, aluminum, or zinc, onto nonflowing electrodes. The metal deposition process usually occurs on the negative electrode side. Although many hybrid RFBs utilize nonaqueous electrolytes to attain high working potential, a zinc-based hybrid system can attain a relatively high working potential in a nonflammable, lower-cost aqueous electrolyte. This is because the zinc/zincate redox couple, $Zn/[Zn(OH)_4]^{2-}$, in a pH 14 alkaline solution has the advantage of a large negative redox potential of −1.23 V versus the standard hydrogen electrode (SHE). An example is the alkaline zinc–ferricyanide hybrid RFB, which was first reported in the 1970s and is still under development.[3] However, the low solubility of the $[Fe(CN)_6]^{3-}/[Fe(CN)_6]^{4-}$ couple at high pH limits the energy density and constrains practical implementation.[4] In addition, acidic zinc–bromine hybrid RFBs have been widely studied and are being commercialized; however, the toxicity and corrosivity of bromine limits widespread deployment.[1]

Recently, redox-active organic and organometallic molecules have been widely studied for their promise of enabling the development of inexpensive flow batteries.[5–7] These molecules exhibit structural diversity and broad tunability, permitting the engineering of solubility, redox potential, kinetics, and stability. Many different types of molecules, including quinones,[8–12] phenazines,[13,14] viologens,[7,15–19] alloxazines,[20] and (2,2,6,6-tetramethylpiperidin-1-yl)oxidanyl,[13,15,16,21,22] have demonstrated good electrochemical performance as redox-active materials in aqueous organic redox flow batteries (AORFBs). Most of these molecules exhibit low reduction potentials and consequently have been explored as negolyte (negative electrolyte) materials. Some exceptions are tetrachloro-1,4 benzoquinone and 4,5-dihydroxybenzene-1,3-disulfonic acid, which have high positive reduction potentials of >0.8 V versus SHE in acidic solution.[9,11,23] Thus, by pairing high potential organic molecules such as these with the $Zn/[Zn(OH)_4]^{2-}$ redox couple, a new type of hybrid RFB can be designed to achieve a high cell voltage.

However, it is difficult to pair an alkaline electrolyte and an acidic electrolyte within conventional single-membrane RFBs due to H^+ or OH^- crossover. Recently, ceramic membranes and bipolar polymer membranes have been introduced into single-membrane pH-differential flow cells, but the high resistance of these membranes has severely limited the current density.[24,25]

Dr. M. Park,[+] Dr. E. S. Beh, E. M. Fell,[++] Dr. D. De Porcellinis, Dr. M.-A. Goulet,[+++] A. A. Wong, Prof. M. J. Aziz
Harvard John A. Paulson School of Engineering and Applied Sciences
29 Oxford Street, Cambridge, MA 02138, USA
E-mail: maziz@harvard.edu

Dr. Y. Jing, E. F. Kerr, Prof. R. G. Gordon
Department of Chemistry and Chemical Biology
Harvard University
12 Oxford Street, Cambridge, MA 02138, USA

Dr. J. Ryu, Prof. J. Cho
Department of Energy Engineering
School of Energy and Chemical Engineering
Ulsan National Institute of Science and Technology (UNIST)
50, UNIST-gil, Ulsan 44919, Republic of Korea
E-mail: jpcho@unist.ac.kr

The ORCID identification number(s) for the author(s) of this article can be found under https://doi.org/10.1002/aenm.201900694.

[+]Present address: Samsung SDI, 467 Beonyeong-ro, Cheonan 31086, Republic of Korea
[++]Present address: Palo Alto Research Center, 3333 Coyote Hill Road, Palo Alto, CA 94304, USA
[+++]Present address: Form Energy, 44 Prince Street, Cambridge, MA 02139, USA

DOI: 10.1002/aenm.201900694

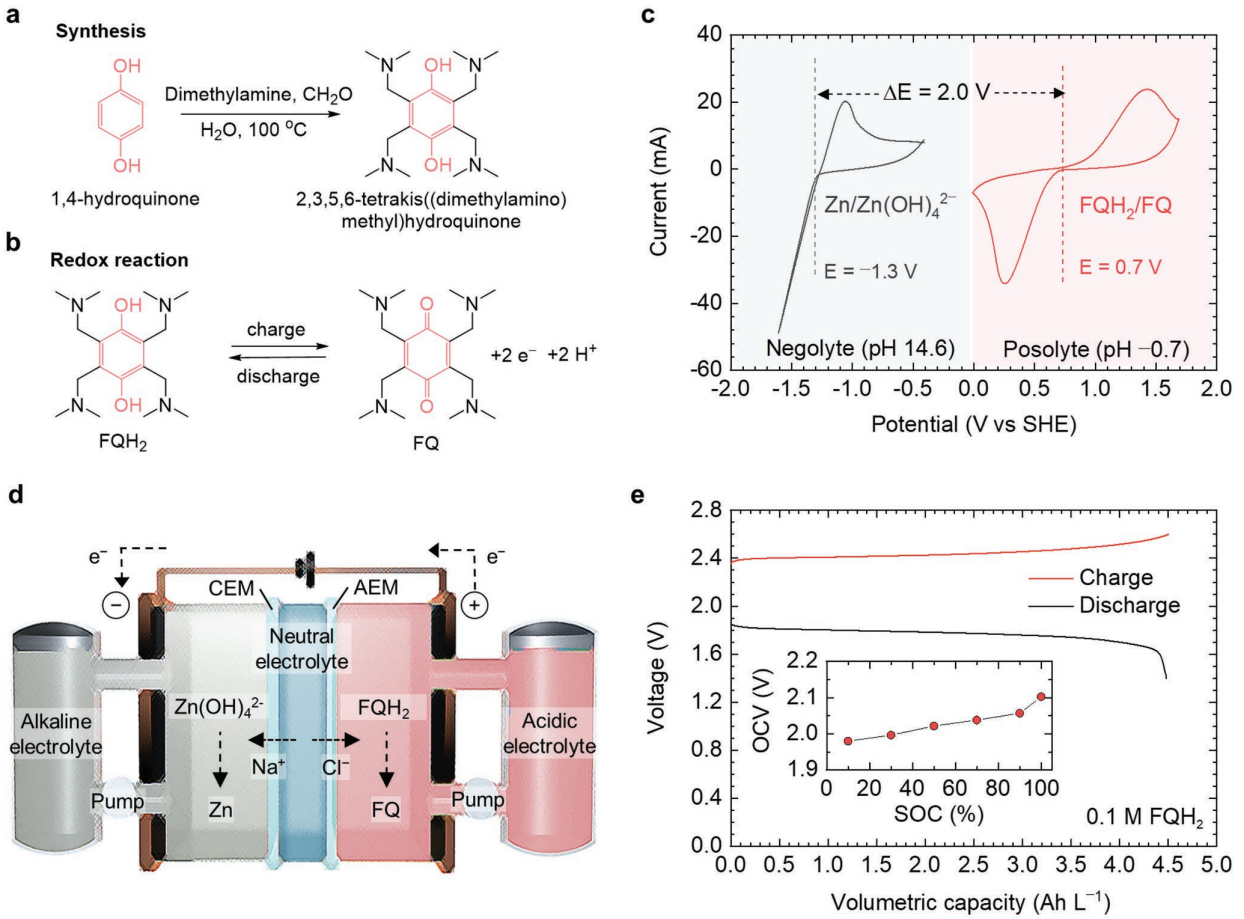

Figure 1. Synthesis and electrochemical characteristics. a) Synthesis of 2,3,5,6-tetrakis((dimethylamino)methyl)hydroquinone (FQH_2) by an electrophilic substitution reaction. b) A two-electron, two-proton process of the FQ molecule. c) Cyclic voltammograms of 0.2 M $[Zn(OH)_4]^{2-}$ and 0.1 M FQH_2 on carbon felt at a scan rate of 50 mV s^{-1} with potential windows from –1.6 to –0.4 V and from 0 to 1.7 V, respectively versus standard hydrogen electrode (SHE). d) A schematic of the aqueous Zn–organic hybrid redox flow batteries with a double-membrane system, showing the charging process (CEM: cation exchange membrane, AEM: anion exchange membrane). e) A charge–discharge voltage profile of the 0.1 M FQH_2 posolyte at a current density of 20 mA cm^{-2} with a voltage window from 1.4 to 2.6 V, where the volumetric capacity was calculated based on the volume of the posolyte. The inset shows cell open-circuit voltage versus state of charge, and all potentials were taken after cell voltage stabilized.

Cell resistance can be reduced considerably by introducing a two-membrane configuration employing an anion exchange membrane (AEM) and a cation exchange membrane (CEM) surrounding a middle electrolyte. This configuration enables a highly customizable, extended selection of redox couples that can operate at different pH values, thereby increasing the cell voltage.[26] For example, Gong et al. recently developed a zinc–iron hybrid RFB with a two-membrane three-electrolyte design using a basic zinc redox couple and an acidic iron redox couple, exhibiting an open-circuit voltage (OCV) of 1.99 V and operating at a current density of 80 mA cm^{-2}.[27]

Here we report the synthesis of a functionalized 1,4-hydroquinone (HQ) with four (dimethylamino)methyl ($–CH_2N(CH_3)_2$) groups and its use as the active species in the posolyte (positive electrolyte) of a two-membrane, three-electrolyte acid–base hybrid RFB. This molecule, 2,3,5,6-tetrakis((dimethylamino)methyl)hydroquinone (FQH_2), exhibits a high solubility of 1.4 M (2.76 M electrons) in H_2SO_4 and can be oxidized in a two-electron, two-proton reaction to a functionalized benzoquinone whose chemical structure with four dimethylamines has a frog-like shape (hereafter referred to as "frog quinone," FQ; see **Figure 1**b). We pair a flowing half-cell of this organic-based posolyte with a $Zn/[Zn(OH)_4]^{2-}$-based negolyte, creating a full cell with an open-circuit voltage of 2.0 V at 50% state of charge (SOC). The theoretical volumetric capacity of the posolyte is 74 Ah L^{-1} and its theoretical energy density when paired with this zinc-based negolyte is 136 Wh L^{-1}, with respect to posolyte volume and 96 Wh L^{-1} with respect to posolyte and minimum required middle electrolyte volume (Section S1.7, Supporting Information). Further, we show that the kinetics and reversibility of this functionalized quinone can be improved by a Ti_4O_7/Ketjenblack (KB) composite catalyst, leading to an acceptable voltage efficiency (VE) at current densities beyond the present limits of cells based on ceramic or bipolar membranes. This work can expand the options for the use of redox-active organic molecules in stationary storage.

2. Results and Discussion

The FQH_2 posolyte is prepared in one step from HQ via the Mannich reaction (Figure 1a; see also Section S1.1, Supporting Information). Briefly, aqueous solutions of dimethylamine and CH_2O were reacted with HQ, followed by the formation of iminium species. This reaction drives an electrophilic aromatic substitution, which is widely established and used for modifying aromatic compounds.[28,29] The molecular weight of the final product 2,3,5,6-tetrakis((dimethylamino)methyl)hydroquinone was 338.24 g mol^{-1}. The ^1H NMR of FQH_2 is presented in Figure S1 in the Supporting Information. The reaction yield was 68%.

Quinones with high reduction potentials are generally susceptible to Michael attack by water while in their oxidized states. This has been identified as a major decomposition pathway for many benzoquinones with unprotected carbons on the aryl ring.[11,30] However, this reaction is suppressed in FQ by replacing all C–H bonds with substituents. FQ is thus not susceptible to decomposition via this mechanism. Although the unsubstituted hydroquinone is insoluble in concentrated acidic solution, we were able to dissolve FQH_2 powder in concentrated sulfuric acid to a concentration of 1.4 M (Figure S2, Supporting Information). The four protonated (dimethylamino) methyl groups become positively charged and act as electron-withdrawing groups, resulting in a relatively high reduction potential for a benzoquinone. The viscosity of the FQ posolyte remains below 10 mPa s for FQ concentrations up to 1 M (Figure S3, Supporting Information); this is in the range of typical aqueous electrolytes.

Figure 1b shows the two oxidation states of FQ/FQH_2. From the Pourbaix diagram of FQ/FQH_2 (Figure S4, Supporting Information), the slope of the redox potential versus pH plot is −59 mV pH^{-1}, which is consistent with a two-electron, two-proton process. There was insufficient solubility to extend the Pourbaix diagram to pH > 5.

The electrochemical behavior of the $Zn/[Zn(OH)_4]^{2-}$ and FQ/FQH_2 redox couples was characterized by cyclic voltammetry (CV), as shown in Figure 1c. The $Zn/[Zn(OH)_4]^{2-}$ redox couple exhibited a redox potential (E) of −1.3 V versus SHE in an alkaline solution of pH 14.6 (4 M NaOH). In strong alkaline solutions (pH > 13) containing zinc, the soluble zincate ion ($[Zn(OH)_4]^{2-}$) is the majority species; this is reduced to metallic zinc on the carbon felt electrode (Figure S5, Supporting Information). We used porous carbon felt electrodes with a volume porosity of ≈95% to suppress the formation of zinc dendrites.[31,32] In an acidic solution with pH −0.4 (FQH_2 dissolved into 2.5 M H_2SO_4 to reach a quinone concentration of 0.1 M), the E of the FQH_2 posolyte was 0.7 V versus SHE, which would yield a cell voltage of 2.0 V by pairing with the $Zn/[Zn(OH)_4]^{2-}$ redox couple.

To effectively combine the acidic FQH_2-based posolyte with the alkaline zincate-based negolyte, we designed an aqueous Zn–organic hybrid RFB as a two-membrane, three-electrolyte system (Figure 1d). Notably, a nonflowing NaCl middle electrolyte was placed between the alkaline negolyte and the acidic posolyte by separating them with the CEM and AEM, respectively; there was an 0.8 mm gap supported by a nylon mesh screen (opening size: 500 µm, wire diameter: 314 µm) between membranes. During the charging process, FQH_2 was oxidized to FQ and chloride ions migrated from the middle electrolyte to the posolyte through the AEM. Simultaneously, $[Zn(OH)_4]^{2-}$ anions were reduced to zinc metal on the carbon felt electrode, and sodium ions moved from the middle electrolyte to the negolyte through the CEM. During discharging, the reverse of this charging process occurs in the battery. Cell testing was performed with a posolyte composed of FQH_2 dissolved into 2.5 M sulfuric acid to reach a quinone concentration of 0.1 M and a negolyte composed of ZnO dissolved into 4 M NaOH to reach a $[Zn(OH)_4]^{2-}$ concentration of 0.2 M. Nafion 117 and Selemion DSV membranes were used as CEM and AEM, respectively, and 3 M sodium chloride served as the middle electrolyte, placed between the two membranes. The cell alternating current (AC) area-specific resistance (ASR) was about 4.4 Ω cm^2 (Figure S6, Supporting Information). Figure 1e shows the charge–discharge voltage profile of the aqueous Zn–organic hybrid RFB during galvanostatic charging and discharging. The OCV was 2.0 V at 50% SOC, the discharge voltage was initially at 1.84 V at a current density of 20 mA cm^{-2}, and the initial discharge capacity was 4.5 Ah L^{-1} based on the posolyte volume.

A series of experiments was performed to investigate the cycling performance of the aqueous Zn–organic hybrid RFB. First, in order to separate the possible issues associated with the new organic posolyte from those of the flow cell itself, we optimized the double-membrane hybrid RFB with the same negolyte but with vanadium as the posolyte (see Section S1, Supporting Information). In the Zn–V hybrid RFB, the alkaline $Zn/[Zn(OH)_4]^{2-}$ negolyte and the acidic VO^{2+}/VO_2^+ posolyte were used. This Zn–V RFB is expected to yield a cell voltage of 2.3 V, as indicated by the CV curves (Figure S7a, Supporting Information). The charge–discharge voltage profile (Figure S7b, Supporting Information) shows a typical galvanostatic process with a discharge capacity of 2.2 Ah L^{-1}. Next, we cycled the Zn–V hybrid RFB at a current density of 20 mA cm^{-2}. At this current density, the battery exhibited 99.95% capacity retention per cycle and 2.90% capacity fade per day (Figure S7c, Supporting Information). The round-trip energy efficiency (EE) is the product of the Coulombic efficiency (CE) and round-trip VE. The initial EE and VE values were 74.3% and 74.5% (Figure S7d, Supporting Information). Notably, the average Coulombic efficiency was 99.9% for 100 cycles, indicating negligible side reactions and a low rate of vanadium crossover during cycling. We found that a negolyte comprising 0.2 M ZnO dissolved into 4 M NaOH (yielding 0.2 M $[Zn(OH)_4]^{2-}$ in 3.6 M NaOH) and a middle electrolyte comprising 3 M NaCl yields stable cycling behavior. It is noteworthy that several other zinc–hybrid RFBs also demonstrate good performance using similar negolyte and middle electrolyte chemistries.[24,26,27] This result confirms the reliability of the double-membrane cell architecture for evaluating the FQH_2 posolyte.

In the aqueous Zn–organic hybrid RFB, test conditions were identical to those of the Zn–V hybrid RFB, except that the same molecular molarity results in a doubling of the posolyte volumetric capacity due to the two-electron nature of the quinone redox process. **Figure 2**a shows the cycling behavior of 0.1 M FQH_2 at a current density of 20 mA cm^{-2} with voltage limits of 1.4 V on discharging and 2.6 V on charging. The initial

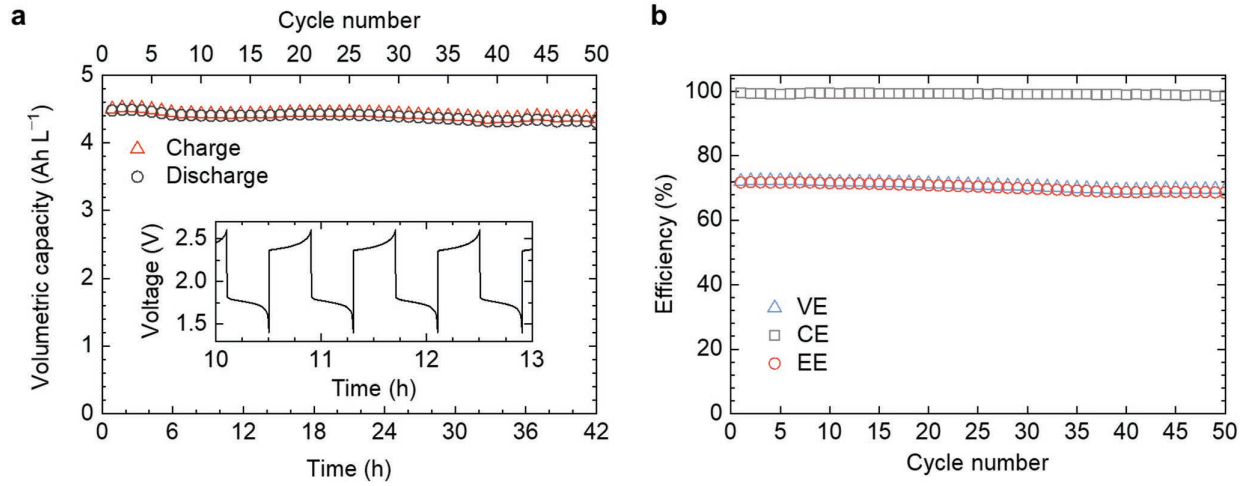

Figure 2. Cycle performance and efficiency. a) Cycling test of a posolyte composed of FQH_2 dissolved into 2.5 M sulfuric acid to reach a quinone concentration of 0.1 M and a negolyte composed of ZnO dissolved into 4 M NaOH to reach a $[Zn(OH)_4]^{2-}$ concentration of 0.2 M, showing the volumetric capacity accessed. The inset shows a voltage versus time curve at a current density of 20 mA cm^{-2} with a voltage ranging from 1.4 to 2.6 V. b) The Coulombic, round-trip voltage efficiency and round-trip energy efficiency (CE, VE, and EE) for 50 cycles. All volumetric capacities were calculated based on the volume of each posolyte, and all tests were carried out without electrocatalysts.

volumetric discharge capacity was 4.5 Ah L^{-1}; the theoretical volumetric capacity is 5.36 Ah L^{-1}. It showed stable cycling performance for 50 cycles, corresponding to 42 h with 99.92% capacity retention per cycle or 97.78% capacity retention per day. The initial Coulombic efficiency was 99.5%, indicating a high reversible capacity of the FQH_2 posolyte. The average values of round-trip energy and voltage efficiency were 70.2% and 70.8%, respectively.

Although the FQ/FQH_2 redox couple cycled stably, its redox kinetics appeared sluggish, with a large potential separation in CVs (Figure 1c); the slow kinetics are expected to decrease the voltage efficiency by creating large cell overpotentials. Thus, we introduced electrocatalysts into the FQH_2 electrode. We utilized KB carbon nanoparticles, with an average diameter of 50 nm (**Figure 3**a). The KB has a specific surface area of around 1400 m^2 g^{-1} and can provide a high density of redox active sites.[33,34] In addition, we explored the use of the Magnéli phase of titanium oxide with a formula of Ti_4O_7, which is considered a promising conductive oxide for electrochemical applications, as a catalyst support.[35] The electronic conductivity of Ti_4O_7 has been reported to be around 1000 S cm^{-1} at room temperature, and its corrosion resistance in acidic electrolytes is also excellent.[36,37] We employed commercial Ti_4O_7 particles (Magneli Materials W-94 micro fine grade powder) with an average feature size of 100 nm (Figure S8, Supporting Information); its crystal phase is presented in Figure S9 in the Supporting Information. To improve the catalytic behavior and electrical conductivity, KB nanoparticles were dispersed on the Ti_4O_7, forming an interconnected structure (Figure 3b).

The results of CV evaluation of the FQH_2 posolyte on glassy carbon are reported in Figure S10 in the Supporting Information. The catalytic activity of Ti_4O_7 without KB was low; however, KB without Ti_4O_7 led to improved reversibility, with the peak separation reduced to 70 mV. Moreover, the Ti_4O_7/KB composite significantly enhanced the reversibility of the FQ/FQH_2 redox couple, reducing the peak separation to 35 mV (Figure 3c). This result shows that the sluggish redox reaction kinetics of the organic compound can be enhanced by the electrocatalyst. The mass transfer behavior of the Ti_4O_7/KB composite was studied by plotting the peak current density as a function of the square root of scan rate, according to the Randles–Sevcik equation (Figure 3d). The peak current density increased linearly with the square root of the scan rate over the range 40 to 100 mV s^{-1}, with R^2 close to 1 (Figure 3e), suggesting that a diffusion process controls the FQH_2 redox reaction on Ti_4O_7/KB composite.

The rate capability of the aqueous Zn–organic hybrid RFB with Ti_4O_7/KB composite catalyst was investigated by varying the current density from 15 to 40 mA cm^{-2} during galvanostatic charging and discharging. A composite-catalyst layer was coated on the carbon felt electrode with a loading of ≈6 mg cm^{-2} (Section S1.5 and Figure S11, Supporting Information). The AC ASR of the cell was about 3.7 Ω cm^2 (Figure S12, Supporting Information). The cell without the catalyst exhibited a larger overvoltage at all current densities and a more strongly decreasing discharge capacity with increasing current density than did the cell with the catalyst (**Figure 4**a,b). The effect of the composite catalyst on performance is most apparent in the dependence of the energy discharged per liter of posolyte on current density at high current density, as shown in Figure 4c. Figure 4d presents the dependence upon current density of VE and CE. The CE of cells with and without catalyst was always over 99.0%. However, the VE of the cell containing Ti_4O_7/KB composite catalyst was higher than that of the flow cell without catalyst at all current densities. Scanning electron microscopy (SEM) showed no obvious change to the catalyst/felt morphology before and after cycling (Figure S13, Supporting Information). We also carried out a high concentration FQ cycling test with FQH_2 dissolved into 2.5 M sulfuric acid to reach a quinone concentration of 0.5 M, which showed a volumetric

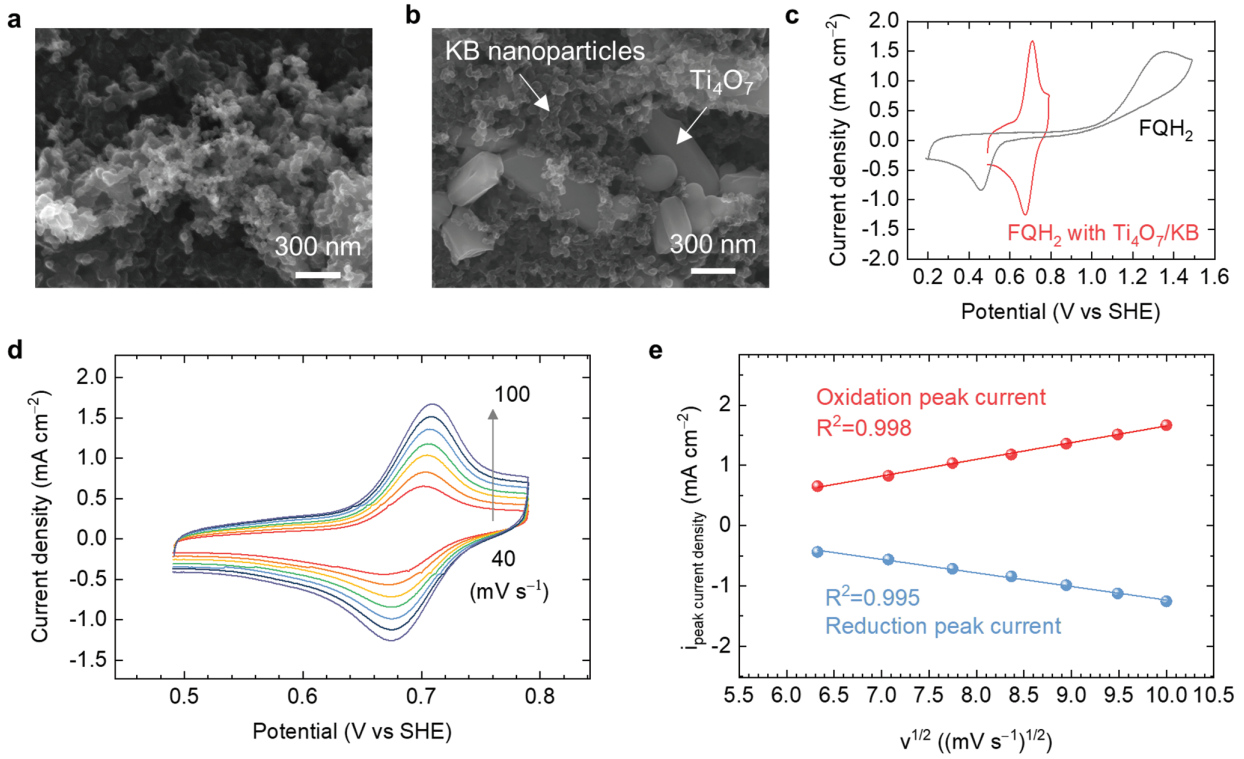

Figure 3. Electrocatalyst for improving FQH_2 kinetics. Scanning electron microscopy (SEM) image of a) Ketjenblack (KB) carbon nanoparticles and b) Ti_4O_7/KB composite. c) Cyclic voltammetry curves (CVs) of the 10×10^{-3} M FQH_2 on the pristine (black line) and Ti_4O_7/KB composite (red line) coated glassy carbon electrodes in 1 M H_2SO_4. d) CVs of the 10×10^{-3} M FQH_2 on the Ti_4O_7/KB composite coated glassy carbon electrodes at different scan rates ranging from 40 to 100 mV s^{-1} and e) the Randles–Sevcik plot obtained from the CV data.

capacity of 22 Ah L^{-1} and a power density of 153 mW cm^{-2} a current density of 130 mA cm^{-2} (Figure S14, Supporting Information); these compare to values of 97.8 mW cm^{-2} at a current density of 96.8 mA cm^{-2} for the 0.1 M FQ cell (Figure S21, Supporting Information).

Whenever one considers a cell with a pH differential across it, one must be concerned with pH leakage, i.e., proton and hydroxide crossover, as a degradation mechanism. Although the AEM and CEM are designed to selectively transport anions and cations respectively while excluding ions of the opposite charge, the selectivity is imperfect.[38] This results in a loss of Coulombic efficiency and the gradual pH decrease of the basic negolyte and the pH increase of the acidic posolyte, leading to a decrease in cell voltage. The trajectory of the pH of the initially neutral middle electrolyte depends on which of the two membranes has more rapid pH leakage. We measured the pH changes of the negolyte, middle electrolyte, and posolyte upon cycling (Figure S15, Supporting Information). The pH of the middle electrolyte decreased during cycling, which implies that proton leakage across the AEM overwhelms hydroxide leakage across the CEM. In Section S2 in the Supporting Information, we estimate the loss current from pH leakage from each electrolyte, resulting in a loss current of 4.64 mA cm^{-2}. In principle the pH leakage can be reversed, at some energy cost, by plumbing the electrolytes exiting the cell into a pH restoring device composed of a salt-splitting cell, which is an established technology for producing alkaline and acidic solutions from salt water.[39,40] In this way, the loss of pH differential and of Coulombic efficiency of the cell from pH leakage can be restored at the cost of system round-trip energy efficiency and the capital cost of the pH restoring device. In the Supporting Information we estimate the thermodynamic minimum energy penalty incurred in running a pH restoring cell. Although the numerical values introduced are specific to the Zn–organic hybrid RFB whose performance is reported in Figure 2, the approach is applicable to all cells operating with a pH differential—except that it is unnecessary for those with ceramic membranes exhibiting negligible pH leakage.

We also observed a gradual decrease in the charge and discharge voltages upon cycling (Figure S16, Supporting Information). To probe the cell voltage changes, the CV of each electrolyte on glassy carbon was recorded after 50 cycles. The Zn/$[Zn(OH)_4]^{2-}$ redox potential showed a positive shift and the oxidation peak of the FQH_2 posolyte was negatively shifted (Figure S17a,b, Supporting Information). We attribute both of these effects to drifts in the pH of the electrolytes. For instance, if the pH of the acidic FQH_2 posolyte increases, the reduction potential of FQ decreases, as shown in the Pourbaix diagram of Figure S3 in the Supporting Information. Likewise, if the pH of the alkaline zincate-bearing negolyte decreases, the reduction potential of the electrode reaction $[Zn(OH)_4]^{2-} + 2e^- \rightarrow Zn(s) + 4OH^-$ should increase. Thus, the shift of redox potential in the CVs is evidence for pH leakage across the membranes.

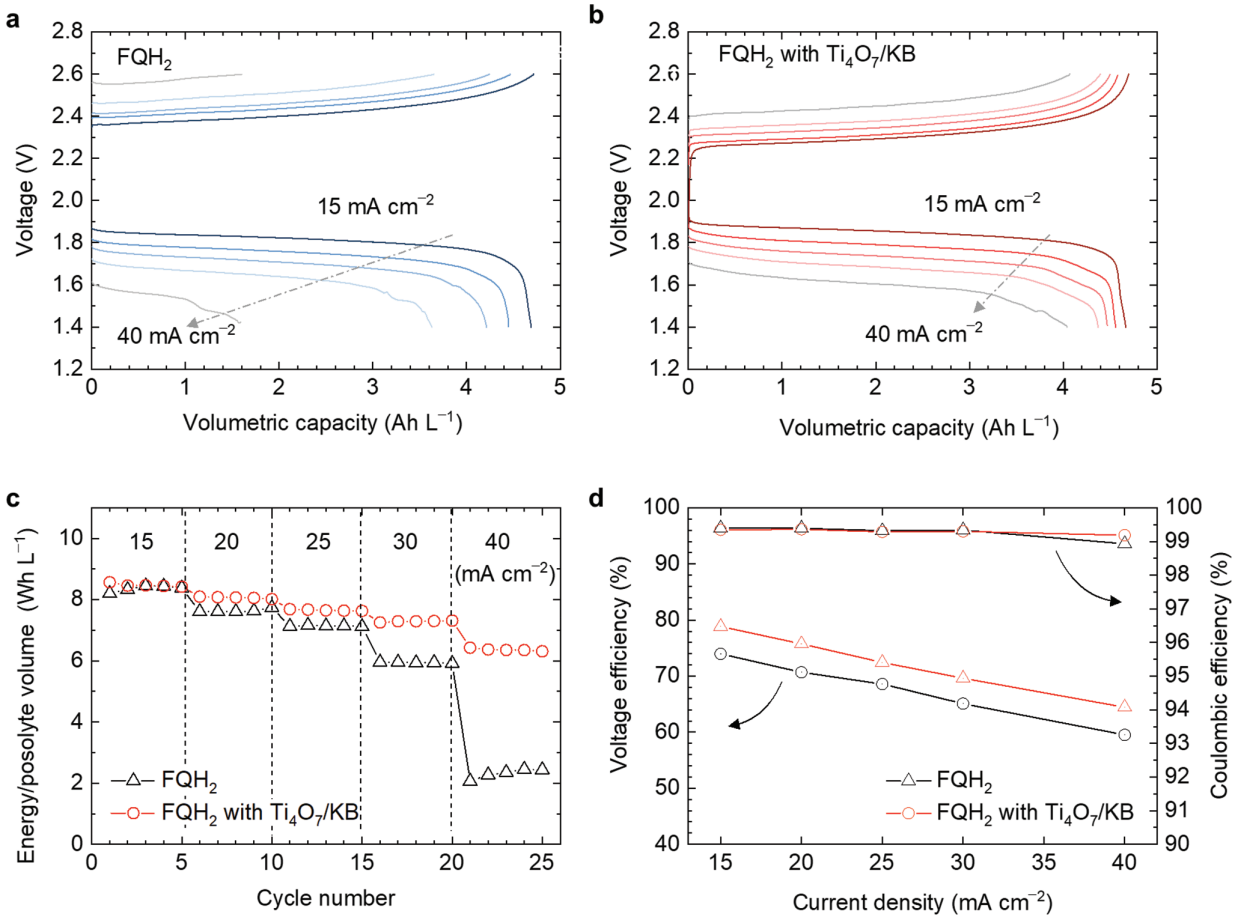

Figure 4. Full cell charge–discharge voltage profiles with the posolyte composed of FQH_2 dissolved into 2.5 M sulfuric acid to reach a quinone concentration of 0.1 M a) with the pristine carbon felt and b) with the Ti_4O_7/KB composite coated carbon felt at different current densities ranging from 15 to 40 mA cm^{-2}. Rate capability of the same cell showing c) energy discharged per liter of posolyte while increasing the current density every five cycles and d) voltage and Coulombic efficiencies at different current densities. In all flow cell tests, the catalyst was used only on the posolyte side. All negolytes were composed of ZnO dissolved into 4 M NaOH to reach a $[Zn(OH)_4]^{2-}$ concentration of 0.2 M.

In addition, the decrease in peak current in the negolyte CV might be the result of dissolved zinc-bearing redox species crossing the CEM from the negolyte to the middle electrolyte. The CVs of middle electrolyte were measured in both negative and positive potential windows. In the negative scan, the reduction peak of $[Zn(OH)_4]^{2-}$ was observed, whereas no such peak was observed for the pristine middle electrolyte (Figure S17c, Supporting Information). This result is consistent with previous reports of the crossover of zincate ions through a Nafion 117 membrane.[41] In contrast, the FQ/FQH_2 redox peak was not observed in the cycled middle electrolyte (Figure S17d, Supporting Information), which is consistent with the low permeability of FQH_2 through the AEM, which we measure to be 2.71×10^{-11} cm^2 s^{-1} (Figure S18, Supporting Information). Although the posolyte is the capacity-limiting side, meaning that an excessive amount of the negolyte was used, these results indicate that the origin of the capacity fade cannot be from the crossover of FQ or FQH_2. ^1H NMR analysis of the cycled posolyte (Figure S19, Supporting Information) indicates chemical decomposition occurs: there were additional peaks in 0.1 M FQH_2 posolyte after 50 charge–discharge cycles, indicating a decomposition product that has not been identified but is similar in structure to the starting material with uncharacterized redox activity. Accordingly, we have identified three degradation mechanisms of the aqueous Zn–organic hybrid RFB: pH leakage, zincate ion crossover and decomposition of the organic compound. Advances in membrane permselectivity will facilitate solutions to the first two problems and advances in understanding and enhancing organic stability will be required for solving the third problem.[42] Other technical challenges and opportunities with the zinc electrode have been the subject of extensive research.[43,44]

3. Conclusion

In conclusion, we have introduced the aqueous Zn–organic hybrid RFB. The pH differential full cell with the

double-membrane, three-electrolyte configuration affords a high cell voltage of 2.0 V at 50% SOC, which is comparable to those of other double-membrane flow batteries (Table S1, Supporting Information). The FQH_2 compound, synthesized by functionalizing hydroquinone with four solubilizing and electron-withdrawing dimethylamine groups under acidic conditions, exhibits a high solubility of 1.4 M (2.76 M electrons) in H_2SO_4. The FQ/FQH_2 couple exhibits a relatively high redox potential, for aqueous-soluble organics, of 0.7 V versus SHE at pH –0.4. Upon pairing the FQ/FQH_2 posolyte with the $Zn/[Zn(OH)_4]^{2-}$ negolyte, the cell cycles with 99.78% capacity retention per day (99. 92% per cycle). We found that sluggish redox kinetics of FQH_2 can be improved by using a Ti_4O_7/KB composite electrocatalyst, resulting in the improved rate capability. Further analysis revealed three degradation mechanisms that will have to be solved for a successful technology to evolve from it. In particular, we estimated that pH leakage could be mitigated by salt splitting and outlined the improvements in membrane properties that would be necessary to make this process practical. The use of organic compounds in acid–alkaline hybrid flow cells provides new opportunities for the design of aqueous RFBs.

Supporting Information

Supporting Information is available from the Wiley Online Library or from the author.

Acknowledgements

This research was supported by U.S. Department of Energy (DOE) award DE-AC05-76RL01830 through Pacific Northwest National Laboratory (PNNL) subcontract 428977, by Innovation Fund Denmark via the Grand Solutions project "ORBATS" File No. 7046-00018B and by the Massachusetts Clean Energy Technology Center. M.P. and J.C. were supported by the 2018 Research Fund (1.180019.01) of Ulsan National Institute of Science and Technology (UNIST). The authors thank Prof. Sung You Hong and Dr. David G. Kwabi for helpful discussions.

Conflict of Interest

The authors declare no conflict of interest.

Keywords

aqueous flow batteries, electrocatalysts, energy storage, quinone, zinc

Received: February 28, 2019
Revised: May 2, 2019
Published online:

[1] G. L. Soloveichik, *Chem. Rev.* **2015**, *115*, 11533.
[2] W. Wang, V. Sprenkle, *Nat. Chem.* **2016**, *8*, 204.
[3] G. B. Adams, R. P. Hollandsworth, B. D. Webber, Report No. LMSC-D-678426 United States NTIS, Lockheed Missiles and Space Co., Palo Alto, CA (USA), Lockheed Palo Alto Research Lab., **1979**.
[4] S. Selverston, R. F. Savinell, J. S. Wainright, *J. Electrochem. Soc.* **2017**, *164*, A1069.
[5] S. Muench, A. Wild, C. Friebe, B. Haupler, T. Janoschka, U. S. Schubert, *Chem. Rev.* **2016**, *116*, 9438.
[6] J. Winsberg, T. Hagemann, T. Janoschka, M. D. Hager, U. S. Schubert, *Angew. Chem., Int. Ed.* **2017**, *56*, 686.
[7] P. Leung, A. A. Shah, L. Sanz, C. Flox, J. R. Morante, Q. Xu, M. R. Mohamed, C. Ponce de León, F. C. Walsh, *J. Power Sources* **2017**, *360*, 243.
[8] B. Huskinson, M. P. Marshak, C. Suh, S. Er, M. R. Gerhardt, C. J. Galvin, X. Chen, A. Aspuru-Guzik, R. G. Gordon, M. J. Aziz, *Nature* **2014**, *505*, 195.
[9] B. Yang, L. Hoober-Burkhardt, F. Wang, G. K. Surya Prakash, S. R. Narayanan, *J. Electrochem. Soc.* **2014**, *161*, A1371.
[10] K. Lin, Q. Chen, M. R. Gerhardt, L. Tong, S. B. Kim, L. Eisenach, A. W. Valle, D. Hardee, R. G. Gordon, M. J. Aziz, M. P. Marshak, *Science* **2015**, *349*, 1529.
[11] B. Yang, L. Hoober-Burkhardt, S. Krishnamoorthy, A. Murali, G. K. S. Prakash, S. R. Narayanan, *J. Electrochem. Soc.* **2016**, *163*, A1442.
[12] Z. Yang, L. Tong, D. P. Tabor, E. S. Beh, M.-A. Goulet, D. De Porcel linis, A. Aspuru-Guzik, R. G. Gordon, M. J. Aziz, *Adv. Energy Mater.* **2017**, *8*, 1702056.
[13] J. Winsberg, C. Stolze, S. Muench, F. Liedl, M. D. Hager, U. S. Schubert, *ACS Energy Lett.* **2016**, *1*, 976.
[14] A. Hollas, X. Wei, V. Murugesan, Z. Nie, B. Li, D. Reed, J. Liu, V. Sprenkle, W. Wang, *Nat. Energy* **2018**, *3*, 508.
[15] T. Janoschka, S. Morgenstern, H. Hiller, C. Friebe, K. Wolkersdorfer, B. Haupler, M. D. Hager, U. S. Schubert, *Polym. Chem.* **2015**, *6*, 7801.
[16] T. Liu, X. Wei, Z. Nie, V. Sprenkle, W. Wang, *Adv. Energy Mater.* **2016**, *6*, 1501449.
[17] E. S. Beh, D. De Porcellinis, R. L. Gracia, K. T. Xia, R. G. Gordon, M. J. Aziz, *ACS Energy Lett.* **2017**, *2*, 639.
[18] C. DeBruler, B. Hu, J. Moss, X. Liu, J. Luo, Y. Sun, T. L. Liu, *Chem* **2017**, *3*, 961.
[19] B. Hu, Y. Tang, J. Luo, G. Grove, Y. Guo, T. L. Liu, *Chem. Commun.* **2018**, *54*, 6871.
[20] K. Lin, R. Gómez-Bombarelli, E. S. Beh, L. Tong, Q. Chen, A. Valle, A. Aspuru-Guzik, M. J. Aziz, R. G. Gordon, *Nat. Energy* **2016**, *1*, 16102.
[21] J. Winsberg, T. Janoschka, S. Morgenstern, T. Hagemann, S. Muench, G. Hauffman, J.-F. Gohy, M. D. Hager, U. S. Schubert, *Adv. Mater.* **2016**, *28*, 2238.
[22] T. Janoschka, N. Martin, M. D. Hager, U. S. Schubert, *Angew. Chem., Int. Ed.* **2016**, *55*, 14427.
[23] H. Alt, H. Binder, A. Köhling, G. Sandstede, *Electrochim. Acta* **1972**, *17*, 873.
[24] X. Yu, A. Manthiram, *ACS Appl. Energy Mater.* **2018**, *1*, 273.
[25] G.-M. Weng, C.-Y. V. Li, K.-Y. Chan, *Mater. Today Energy* **2018**, *10*, 126.
[26] S. Gu, K. Gong, E. Z. Yan, Y. Yan, *Energy Environ. Sci.* **2014**, *7*, 2986.
[27] K. Gong, X. Ma, K. M. Conforti, K. J. Kuttler, J. B. Grunewald, K. L. Yeager, M. Z. Bazant, S. Gu, Y. Yan, *Energy Environ. Sci.* **2015**, *8*, 2941.
[28] J. F. Bunnett, R. E. Zahler, *Chem. Rev.* **1951**, *49*, 273.
[29] R. F. W. Bader, C. Chang, *J. Phys. Chem.* **1989**, *93*, 2946.
[30] L. Hoober-Burkhardt, S. Krishnamoorthy, B. Yang, A. Murali, A. Nirmalchandar, G. K. Surya Prakash, S. R. Narayanan, *J. Electrochem. Soc.* **2017**, *164*, A600.
[31] B. Li, Z. Nie, M. Vijayakumar, G. Li, J. Liu, V. Sprenkle, W. Wang, *Nat. Commun.* **2015**, *6*, 6303.
[32] Z. Yuan, Y. Duan, T. Liu, H. Zhang, X. Li, *iScience* **2018**, *3*, 40.
[33] J. Ryu, M. Park, J. Cho, *J. Electrochem. Soc.* **2016**, *163*, A5144.
[34] M. Park, J. Ryu, Y. Kim, J. Cho, *Energy Environ. Sci.* **2014**, *7*, 3727.

[35] Y. Shao, J. Liu, Y. Wang, Y. Lin, *J. Mater. Chem.* **2009**, *19*, 46.
[36] P. Geng, J. Su, C. Miles, C. Comninellis, G. Chen, *Electrochim. Acta* **2015**, *153*, 316.
[37] S. You, B. Liu, Y. Gao, Y. Wang, C. Y. Tang, Y. Huang, N. Ren, *Electrochim. Acta* **2016**, *214*, 326.
[38] J. Jörissen, K. H. Simmrock, *J. Appl. Electrochem.* **1991**, *21*, 869.
[39] S. Mazrou, H. Kerdjoudj, A. T. Chérif, J. Molénat, *J. Appl. Electrochem.* **1997**, *27*, 558.
[40] N. Tzanetakis, W. M. Taama, K. Scott, *Filtr. Sep.* **2002**, *39*, 30.
[41] J. Zhang, G. Jiang, P. Xu, A. Ghorbani Kashkooli, M. Mousavi, A. Yu, Z. Chen, *Energy Environ. Sci.* **2018**, *11*, 2010.
[42] D. P. Tabor, R. Gómez-Bombarelli, L. Tong, R. G. Gordon, M. J. Aziz, A. Aspuru-Guzik, *J. Mater. Chem. A* **2019**, https://doi.org/10.1039/C9TA03219C.
[43] S. Higashi, S. W. Lee, J. S. Lee, K. Takechi, Y. Cui, *Nat. Commun.* **2016**, *7*, 11801.
[44] F. Wang, O. Borodin, T. Gao, X. Fan, W. Sun, F. Han, A. Faraone, J. A. Dura, K. Xu, C. Wang, *Nat. Mater.* **2018**, *17*, 543.

SUPPLEMENTARY ONLINE INFORMATION

for

A high voltage aqueous zinc–organic hybrid flow battery

Minjoon Park[1,+], Eugene S. Beh[1,++], Eric M. Fell[1], Yan Jing[2], Emily F. Kerr[2], Diana De Porcellinis[1], Marc-Antoni Goulet[1,+++], Jaechan Ryu[3], Andrew A. Wong[1], Roy G. Gordon[1,2], Jaephil Cho[2,*], Michael J. Aziz[1,*]

[1]Harvard John A. Paulson School of Engineering and Applied Sciences, 29 Oxford Street, Cambridge, MA 02138, USA
[2]Department of Chemistry and Chemical Biology, Harvard University, 12 Oxford Street, Cambridge, MA 02138, USA
[3]Department of Energy Engineering, School of Energy and Chemical Engineering, Ulsan National Institute of Science and Technology (UNIST), 50, UNIST-gil, Ulsan 44919, Republic of Korea.
*E-mail: jpcho@unist.ac.kr, maziz@harvard.edu

[+]Current address: Samsung SDI, 467 Beonyeong-ro, Cheonan, 31086, Republic of Korea.
[++]Current address: Palo Alto Research Center, 3333 Coyote Hill Road, Palo Alto, CA 94304, USA
[+++]Current address: Form Energy, 44 Prince Street, Cambridge, MA 02139, USA

Table of contents

1. Methods

1.1 Synthesis

For the synthesis of 2,3,5,6-tetrakis((dimethylamino)methyl)hydroquinone (FQH_2), 5 grams of 1,4-hydroquinone (45.4 mmol) were added to a 500 mL round bottom flask with 67 mL of 37 weight percent formaldehyde solution (899 mmol) and 136 mL of 40 weight percent dimethylamine in water (1,060 mmol). The reaction was stirred at reflux for 5 hours at 100 °C (oil bath) under nitrogen with a chilled reflux condenser and then vacuum filtered, rinsed with water and dried *in vacuo*. The product was analyzed by ^{1}H NMR without further purification and the final yield was 68%. All chemicals were purchased from Sigma-Aldrich and used as received.

1.2 Characterization

Scanning electron microscopy (SEM) images were taken using a FE-SEM (Ultra55, Zeiss) operating at 1.5 kV. X-ray diffractometry (XRD) was used to analyze the crystalline phase (MiniFlex, Rigaku). A potentionstat (Reference3000, Gamry) and a battery cycler (BCS-815, Bio-Logic) were used to evaluate the electrochemical properties. The viscosity of the FQH_2 posolyte was measured using a viscometer (ViscoLab3000, Cambridge Applied Systems). The pH of the

FQH_2 posolyte was evaluated after cycling by diluting the electrolyte by a factor of 100 and then taking a measurement with a pH meter (pH700, Oakton).

1.3 Permeability Measurements

The permeability of FQH_2 was measured with a lab-made cell. The membrane was sandwiched between two elbowed glass tubes. A 0.1 M solution of FQH_2 in 1 M H_2SO_4 was placed on the donating side and paired with 1 M H_2SO_4 solution of equal volume on the receiving side. To keep the solutions well mixed, the cell was placed on a nutating table. The concentration of FQH_2 in the receiving side was measured at various times using a UV-visible spectrophotometer (UV-Vis, Ocean Optics Flame-S Spectrometer Assembly). For each time point, a 400 μL aliquot of the solution on the receiving was removed, diluted, and its absorbance measured by UV-Vis. The aliquot was immediately replaced by an equal volume of fresh H_2SO_4 solution. The permeability coefficient P was calculated from the following equation:

$$P = \frac{\Delta \ln\left(1 - \frac{2C_{r,n}}{C_0}\right)\left(-\frac{Vl}{2A}\right)}{\Delta t},$$

where $C_{r,n}$ is the crossed-over concentration of the electroactive species at time t_n, C_0 is the active species concentration in the donating reservoir at time 0, V is the volume of the receiving side (4 cm^3), l is the membrane thickness (110 μm), A is the membrane area (0.71 cm^2), t is the time, and Δ indicates a finite difference. The evaluation of $C_{r,n}$ accounts for all the electroactive molecules that have permeated through the membrane, whether or not they have been removed in an aliquot for the UV-Vis measurements.

For the test procedure, the receiving side concentration increases in time. An aliquot is collected n times from the receiving side and measured with UV-Vis; we denote its measured concentration by $C_{b,n}$. The aliquot is replaced by fresh solution (1M H_2SO_4). This dilution reduces the concentration in the receiving solution and keeps the flux from decaying over time. We define the crossed-over concentration, C_r, as the time-integrated flux × area/V, where V is the volume of the receiving side. $C_{r,n}$ is the sum of the concentration measured with the UV-Vis at each time point and the concentration removed for the previous measurements. We evaluate $C_{r,n}$, the crossed-over concentration immediately after the nth measurement, by adding up the concentrations measured from a series of dilutions:

$$C_{r,n} = c_{b,n} + \sum_{k=1}^{n-1} c_{b,k} \frac{V_k}{V}$$

Where $C_{b,k}$ is the concentration measured in the previous point and removed, and V_k is the volume taken from the receiving side for the UV-Vis measurement and replaced with fresh solution.

1.4 Solubility tests

The solubility limit of FQH_2 in H_2SO_4 was measured by adding FQH_2 powder to H_2SO_4 until no further solid could be dissolved. After filtering the mixture through a PTFE 0.45 μm syringe filter, a saturated solution of FQH_2 in H_2SO_4 was obtained. The saturated solution was then diluted by a known amount and the concentration was evaluated by UV-Vis. The concentration was determined by comparing to a calibrated absorbance-concentration curve with known FQH_2 concentrations.

1.5 Electrochemical characterization

The Ti_4O_7/KB composite catalyst was coated on the carbon felt (XF30A, Toyobo) surface. The catalyst ink was prepared by mixing 16 mg KB (EC600JD, Akzo Nobel Chemicals) and 64 mg

Ti_4O_7 powders (W94, Magneli Materials) in the mixture of 80 μL of the binder solution (Nafion® perfluorinated resin solution, 5 wt. % in lower aliphatic alcohols and water, contains 15-20% water, Sigma-Aldrich) and 3,200 μL of ethanol by ultrasonically blending for 30 min. The ~6 mg cm^{-2} of catalyst ink was coated onto a carbon felt, and then dried at 60°C for 1 h. CV measurements were performed using a three-electrode configuration consisting of a glassy carbon working electrode (3 mm diameter), a graphite counter electrode and a Ag/AgCl reference electrode. The electrolytes composed of FQH_2 dissolved into 2.5 M sulfuric acid to reach a quinone concentration of 0.1 M and ZnO dissolved into 4 M NaOH to reach a $[Zn(OH)_4]^{2-}$ concentration of 0.2 M were used. CV data were collected using a potentiostat at different scan rates of 10 to 100 mV s^{-1}. For catalyst tests, 2 μL of catalyst ink was applied on the surface of the glassy carbon disk electrode by the drop-casting method.

1.6 Flow cell tests

One sheet of carbon felt (carbon felt, XF30A, Toyobo Co., volumetric porosity: 95%, thickness: 2 mm) with 5 cm^2 geometric area was used for each of the positive and negative electrodes without pre-treatment. The electrode was placed in lab-made flow cell as in a previous study.[1] Nafion 117 and Selemion DSV ion exchange membranes served as CEM and AEM, respectively. For the pre-treatment, Nafion 117 was immersed in 3 M NaCl solution for 24 hours. The Selemion DSV was used as received, containing mobile Cl^- counterions. A Fumasep E-630(K) membrane, which has a non-fluorinated, sulfonated polyaryletherketone-copolymer backbone, was immersed in 3 M NaCl solution for 24 hours and used for the 0.5 M posolyte test. The middle electrolyte was supported by 800 μm of Teflon gasket and injected by syringe between membrane and gasket. 3 mm of graphite-based plates (Golden Energy Fuel Cell Co., Ltd) with no flow fields were placed between carbon felt electrode and copper current collectors. Galvanostatic cell cycling was performed with current densities varying from 15 to 40 mA cm^{-2} with specified voltage limits. Although potential holding is useful to confirm molecular stability[2], we used the constant current mode in all tests because of the decrease of Coulombic efficiency observed upon cycling (Figure S20), which we hypothesize to be caused by a side reaction on the zincate negolyte at extreme potentials. A Masterflex peristaltic pump (Cole-Parmer) was used to circulate the posolyte through the electrode at a flow rate of 60 mL min^{-1}.

For the 0.1 M vanadium posolyte test, the posolyte was 7 mL of 0.1 M $VOSO_4$ in 2.5 M H_2SO_4. The middle electrolyte was 1.5 mL of 3 M NaCl. 10 mL of negolyte was formed by adding ZnO to 4 M NaOH to a $[Zn(OH)_4]^{2-}$ concentration of 0.2 M.

For the 0.1 M FQH_2 posolyte test, 7 mL of posolyte was formed by adding FQH_2 powder to 2.5 M H_2SO_4 to reach a quinone concentration of 0.1 M. The middle electrolyte was 1.5 mL of 3 M NaCl. 10 mL of negolyte was formed by adding ZnO to 4 M NaOH to reach a $[Zn(OH)_4]^{2-}$ concentration of 0.2 M.

In all cases the posolyte was the capacity-limiting side during both charging and discharging. At the negative electrode, an excess amount of negolyte was used and 0.1 g of granular zinc metal (30 mesh) was placed between two sheets of carbon felt to promote the zinc plating and stripping processes. Polarization curves were acquired by charging the cell to 100% state of charge (SOC), then polarized by linear sweep voltammetry at 5 mV s^{-1}. Potentio-controlled electrochemical

impedance spectroscopy (PEIS) was recorded as needed at frequencies ranging from 10 kHz to 1 Hz.

1.7 Calculation of theoretical energy density

At a maximum solubility of FQH_2, for full charging of 10 mL of 1.4 M FQ, the middle electrolyte needs to transport 10 mL * 1.4 M * 2 e^- = 28 mmol of chloride ions. The maximum solubility of NaCl is known as 6.6 M, so 4.24 mL of middle electrolyte is needed. Its theoretical energy density when paired with this zinc-based negolyte is 136 Wh L^{-1}, with respect to posolyte volume, and 96 Wh L^{-1} with respect to posolyte and minimum required middle electrolyte volume if NaCl composes the middle electrolyte at its solubility limit of 6.6 M.

2. Supporting figures

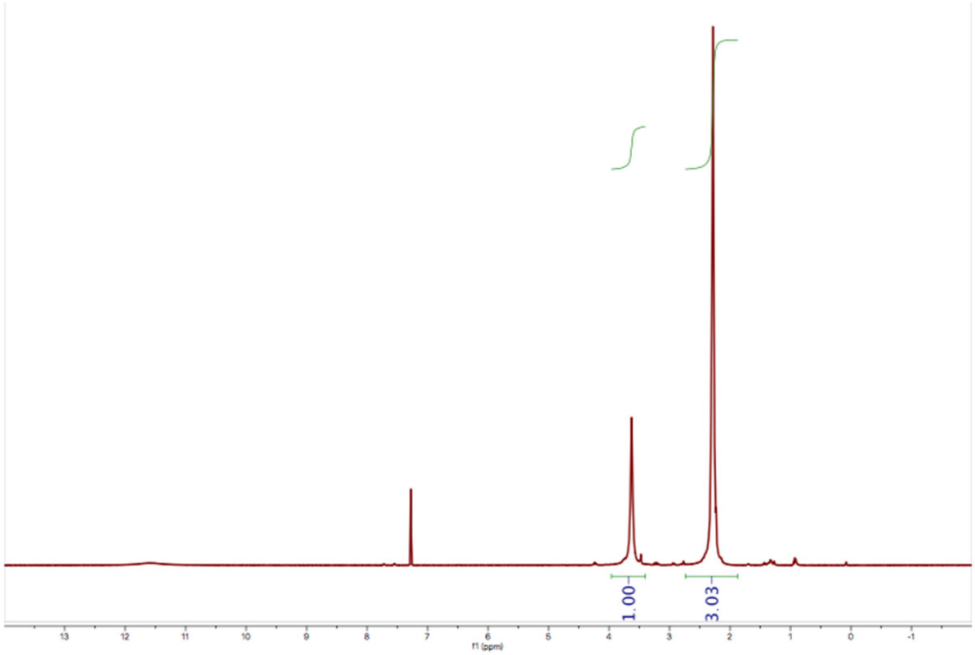

Figure S1. ^{1}H-NMR spectrum of the prepared FQH_2. ^{1}H NMR (500 MHz, $CDCl_3$): δ 3.63 (s, 8H), 2.27 (s, 24H).

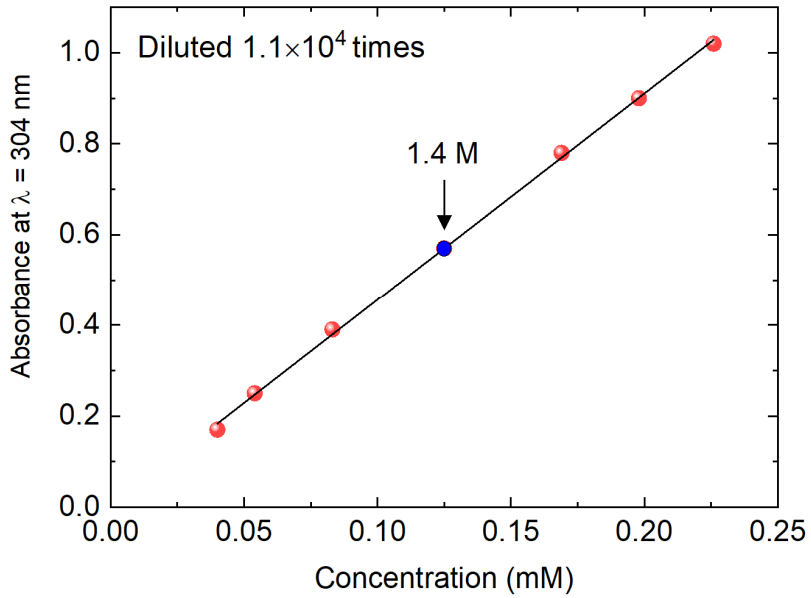

Figure S2. Solubility measurement of FQH_2, showing the maximum solubility of 1.4 M. The solubility limit of FQH_2 was measured in its reduced form by adding FQH_2 powder to 2.5 M H_2SO_4 until no further solid could be dissolved. After filtering the mixture through a polytetrafluoroethylene 0.45 mm syringe filter, a saturated solution of FQH_2 in H_2SO_4 was obtained. The saturated solution was then diluted by a known amount, and the concentration was evaluated by UV-Vis spectrophotometry (absorbance at λ = 304 nm). The concentration was calculated according to a pre-calibrated absorbance-concentration curve of known concentrations of FQH_2 (red points).

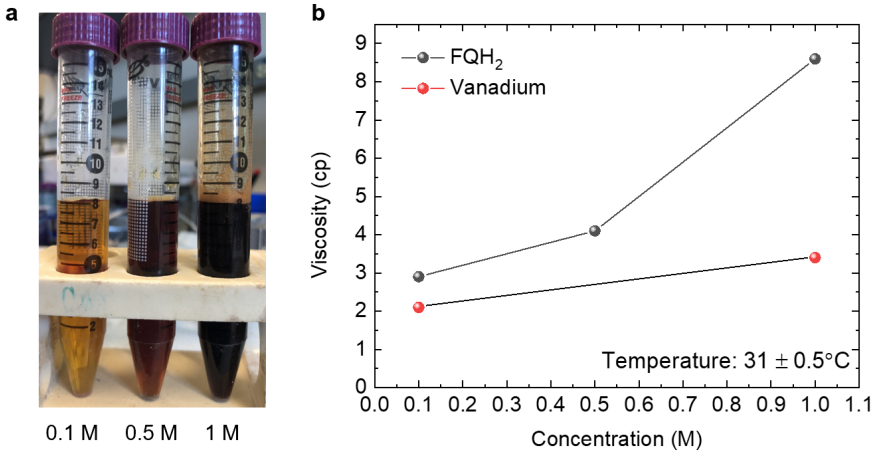

Figure S3. Photographs and viscosity of FQH_2 posolyte at three concentrations. (a) Digital photographs of 0.1, 0.5 and 1.0 M of reduced FQH_2 in H_2SO_4 posolytes and (b) their viscosity values, including the viscosity of 0.1 and 1.0 M of vanadium electrolyte in 2.5 M H_2SO_4. Note FQH_2 electron concentration is twice the molecular concentration.

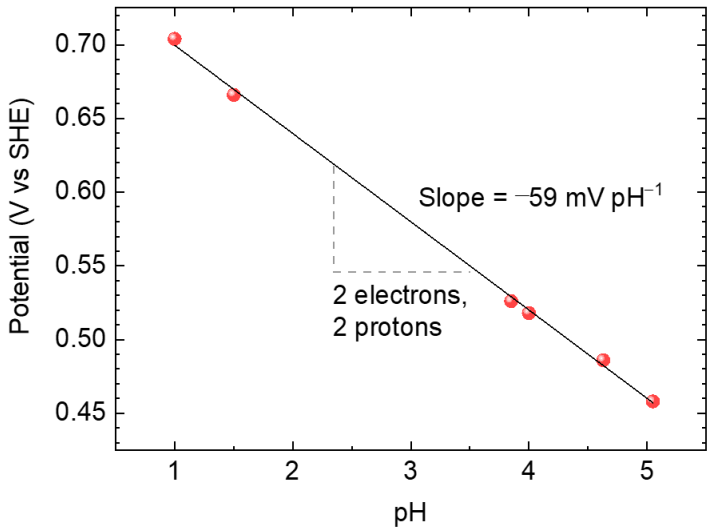

Figure S4. Pourbaix diagram of FQH_2. Solvent/buffer; pH 1, pH 1.5 = sulfuric acid, pH 3.85, 4, 4.63 and 5.05 = acetate buffer. Each individual CV was run with 10 mM FQH_2 and 1 M of buffer. Data are fitted to a solid line indicating a slope of –59 mV pH^{-1}, corresponding to a two-electron, two-proton process.

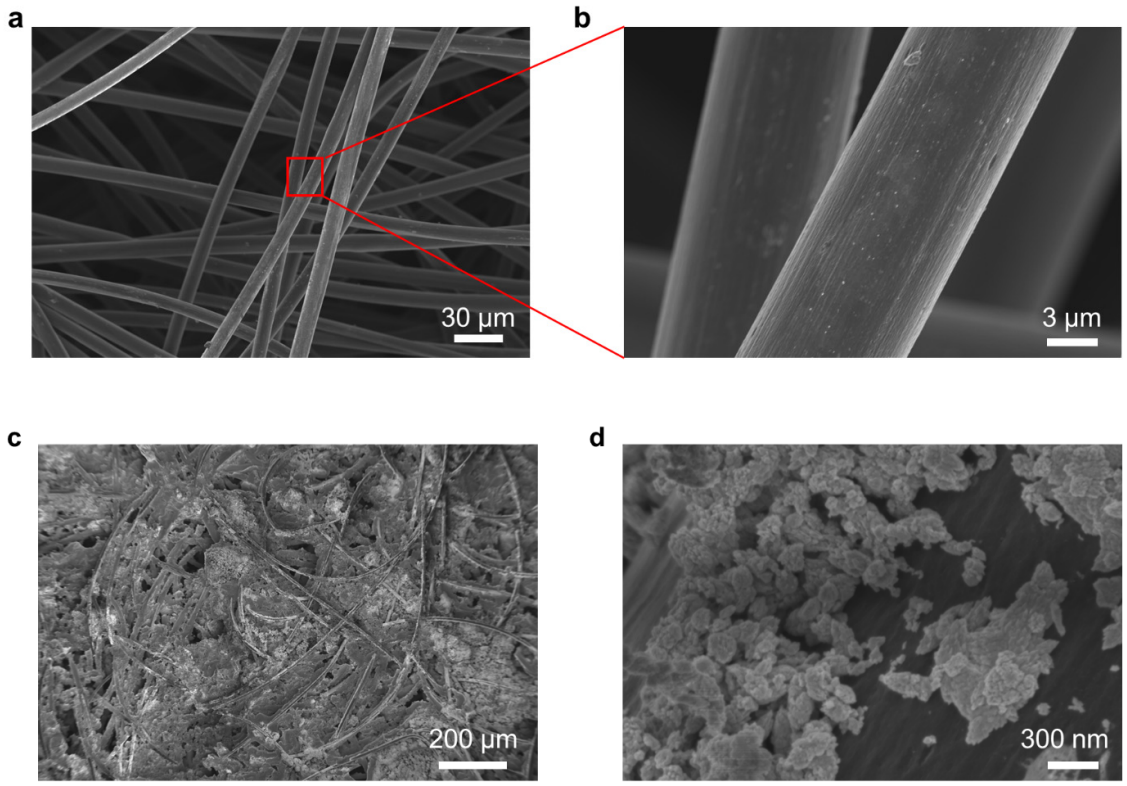

Figure S5. Scanning electron microscopy (SEM) images of (a) the pristine carbon felt and (b) its magnified image, showing a diameter of ~7 µm. SEM images of (c) the zinc plated carbon felt electrode after 50 cycles, and (d) its magnified image, showing that the carbon felt fibers were covered with zinc metal.

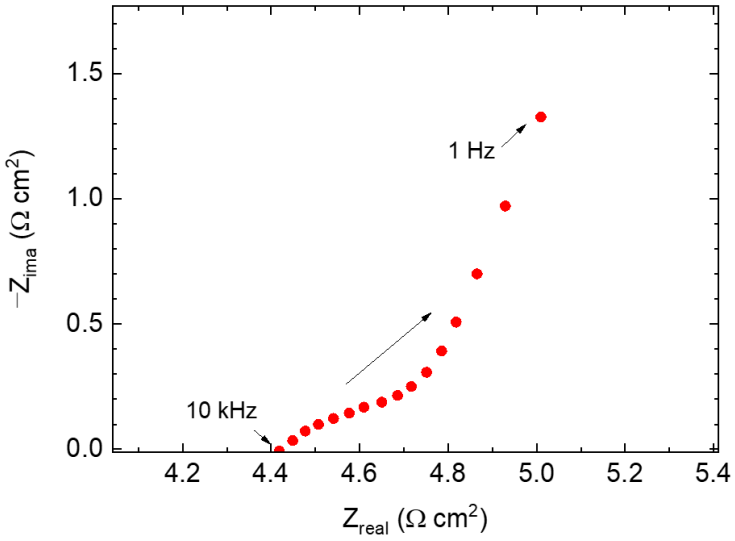

Figure S6. Electrochemical impedance spectroscopy (EIS) of 0.1 M FQH_2 flow cell reported in Figure 1e. The cell AC area-specific resistance (ASR) was ~ 4.4 Ω cm^2. Frequency decreases from left to right.

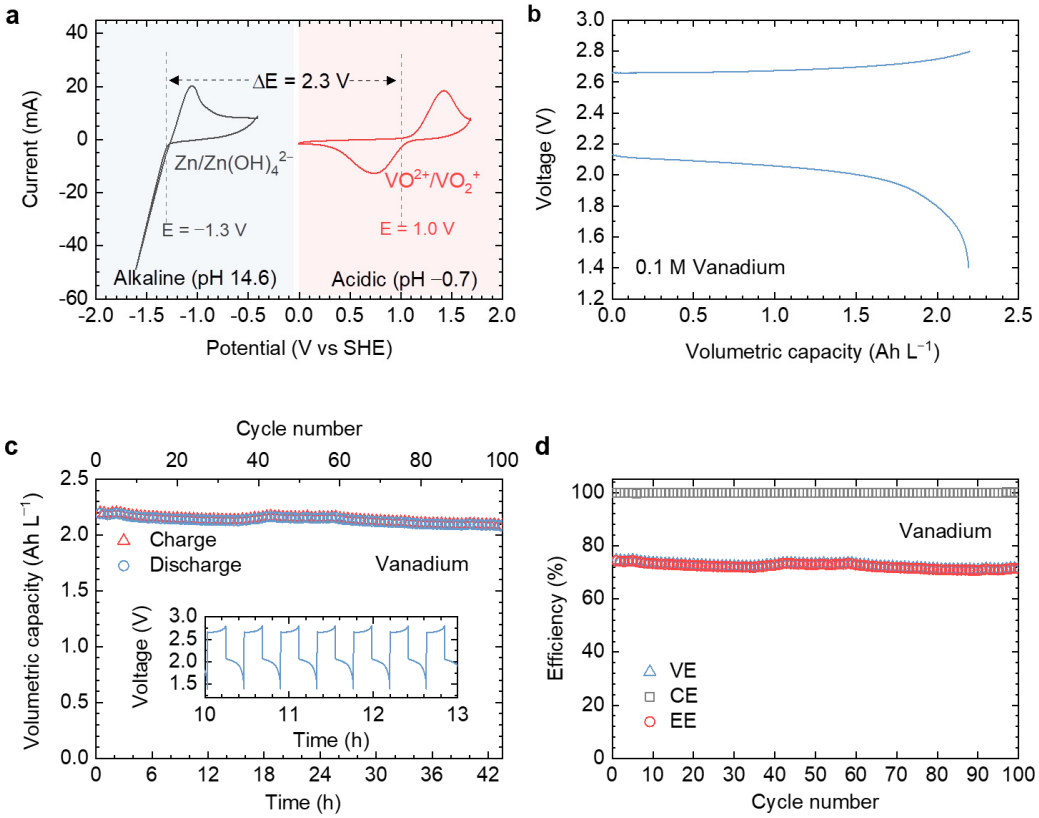

Figure S7. The aqueous Zn-V RFB performance. (a) Cyclic voltammetry of 0.2 M $[Zn(OH)_4]^{2-}$ and 0.1 M VO^{2+} solutions on the carbon felt at a scan rate of 50 mV s^{-1} with potential window from −1.6 to −0.4 V and 0 to 1.7 V versus standard hydrogen electrode (SHE). (b) A voltage profile of the 0.1 M vanadium posolyte at a current density of 20 mA cm^{-2} with cutoff voltage from 1.4 to 2.8 V, where the volumetric capacity was calculated based on the volume of the posolyte. (c) Cycling test of 0.1 M vanadium posolyte in 2.5 M sulfuric acid, showing the volumetric capacity with the inset of voltage versus time curve at a current density of 20 mA cm^{-2} with a voltage ranging from 1.4 to 2.8 V and (d) the Coulombic, round-trip voltage efficiency and round-trip energy efficiency (CE, VE and EE) for 50 cycles. All volumetric capacities were calculated based on the volume of each posolyte, and all tests were carried out without electrocatalysts.

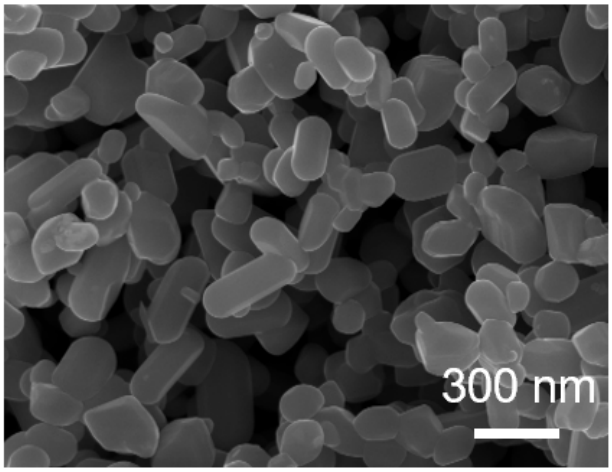

Figure S8. SEM image of the Ti_4O_7 particles with an average feature size of 100 nm.

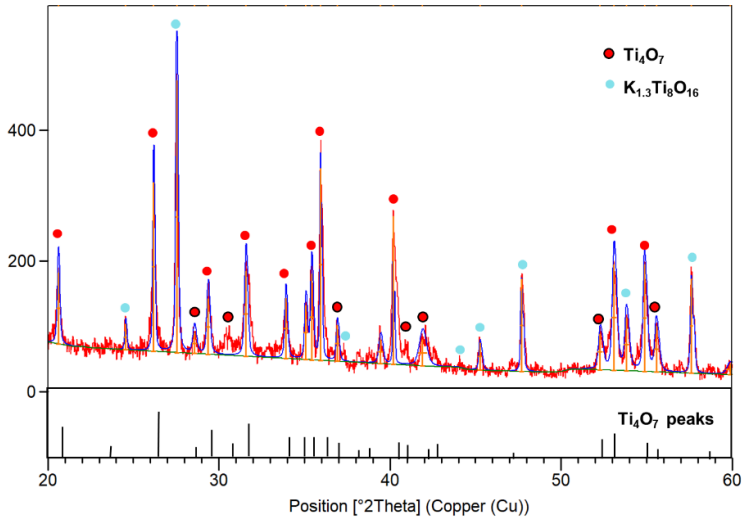

Figure S9. Powder XRD pattern of commercial Ti_4O_7 powder, which consisted of Ti_4O_7 phase with $K_{1.3}Ti_8O_{16}$ impurity.

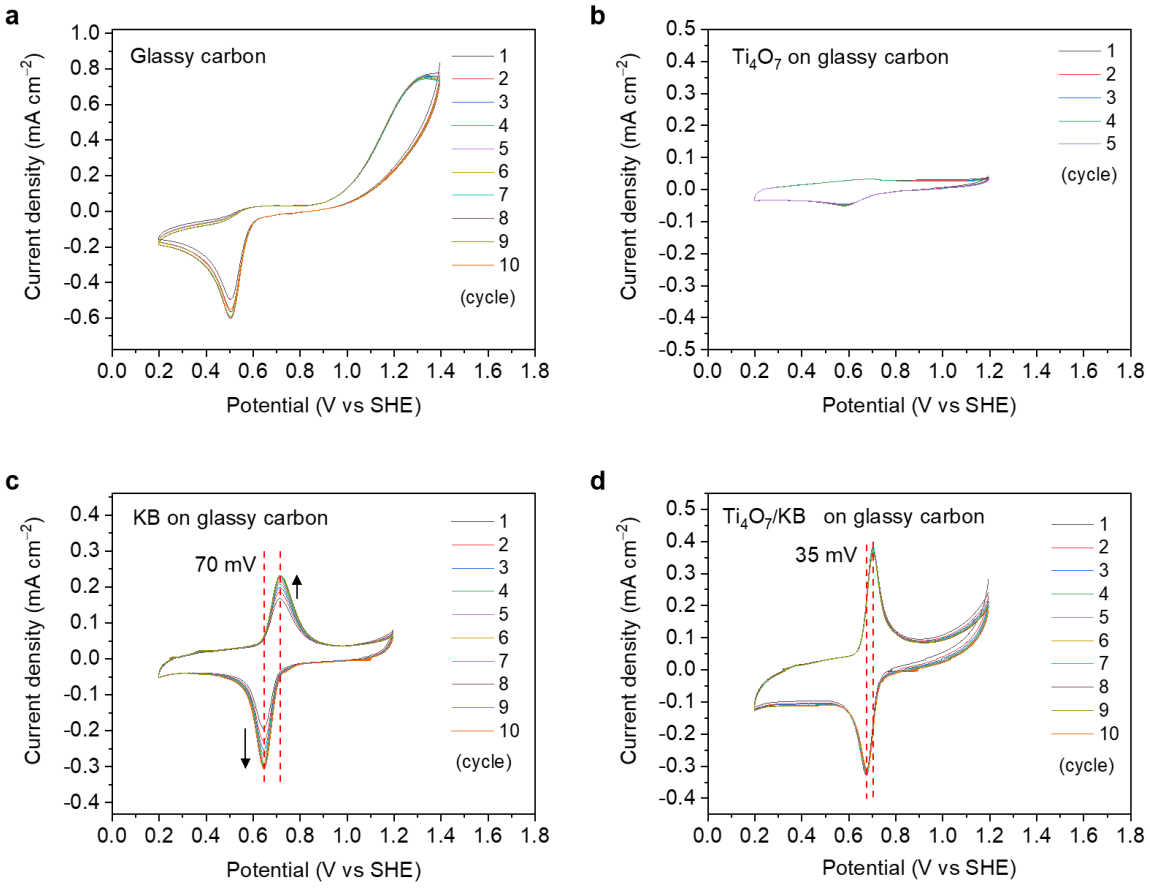

Figure S10. Cyclic voltammetry curves (CVs) of the 10 mM FQH_2 posolyte on (a) the pristine, (b) only Ti_4O_7, and (c) only KB and (d) Ti_4O_7/KB composite coated glassy carbon electrodes at a scan rate of 10 mV s^{-1} for 10 cycles.

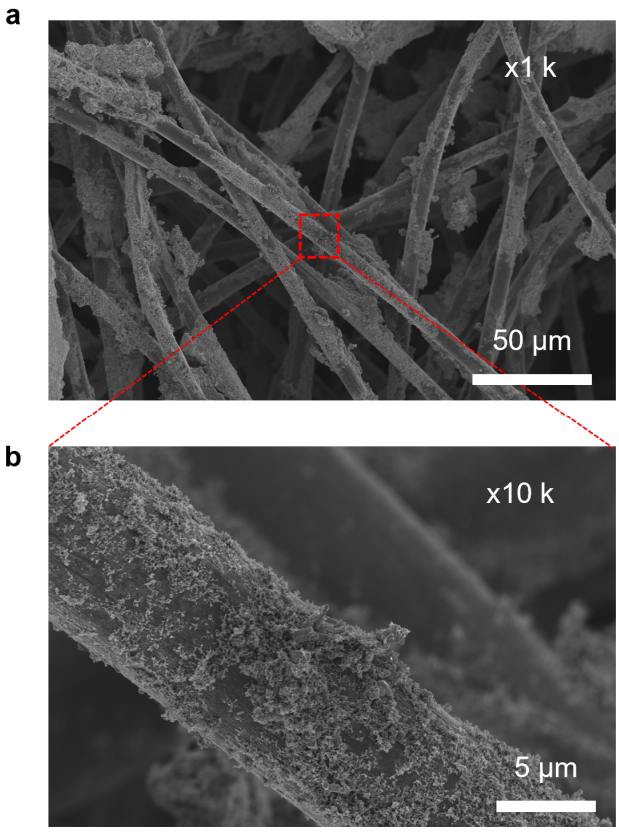

Figure S11. SEM images of (a) Ti_4O_7/KB composite coated carbon felt electrode, and (b) a magnified image. Both images were taken before the cycling test.

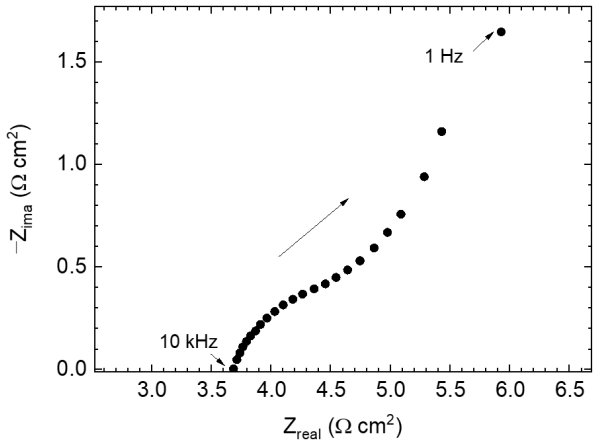

Figure S12. Electrochemical impedance spectroscopy (EIS) of 0.1 M FQH_2 flow cell with Ti_4O_7/KB composite coated carbon felt electrodes reported in Figure 4c. The cell area-specific resistance (ASR) was ~ 3.7 Ω cm^2. Frequency decreases from left to right.

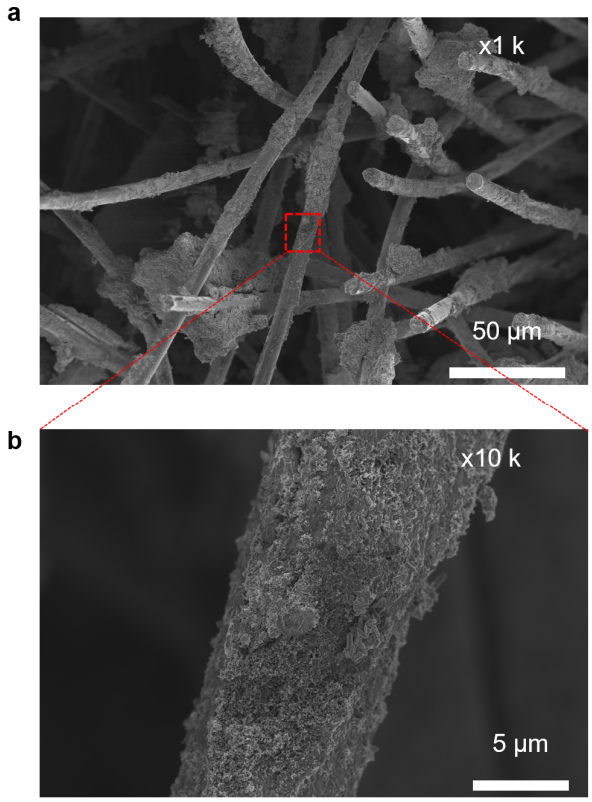

Figure S13. (a) SEM images of post-cycling (55 cycles, 40 h.) Ti_4O_7/KB composite coated carbon felt electrode, and (b) a magnified image after cycling test.

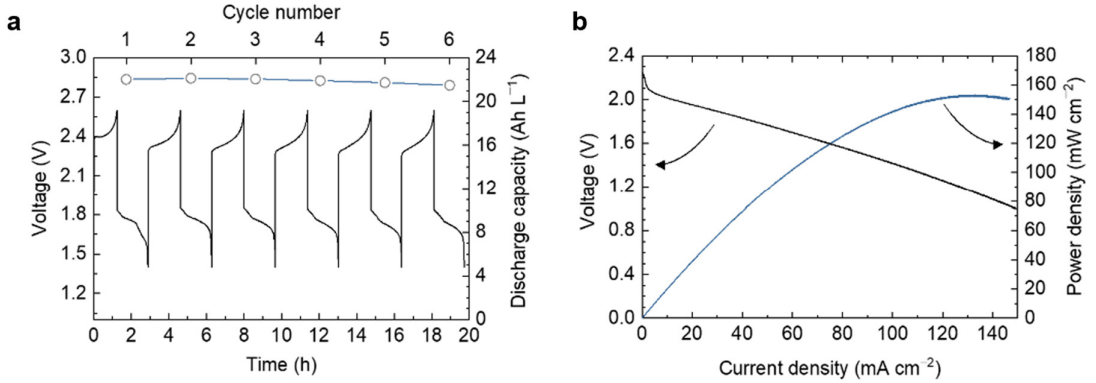

Figure S14. High-concentration aqueous Zn−organic hybrid flow battery performance. Full-cell voltage and power density curves versus current density of 0.5 M FQH_2 posolyte (1 M e^-) in a fully charged state. Voltage vs. time curves and discharge capacity of 0.5 M FQH_2 posolyte at a current density of 20 mA cm^{-2}. All flow cell data were obtained using Ti_4O_7/KB catalyst coated carbon felt that was used only on the posolyte side.

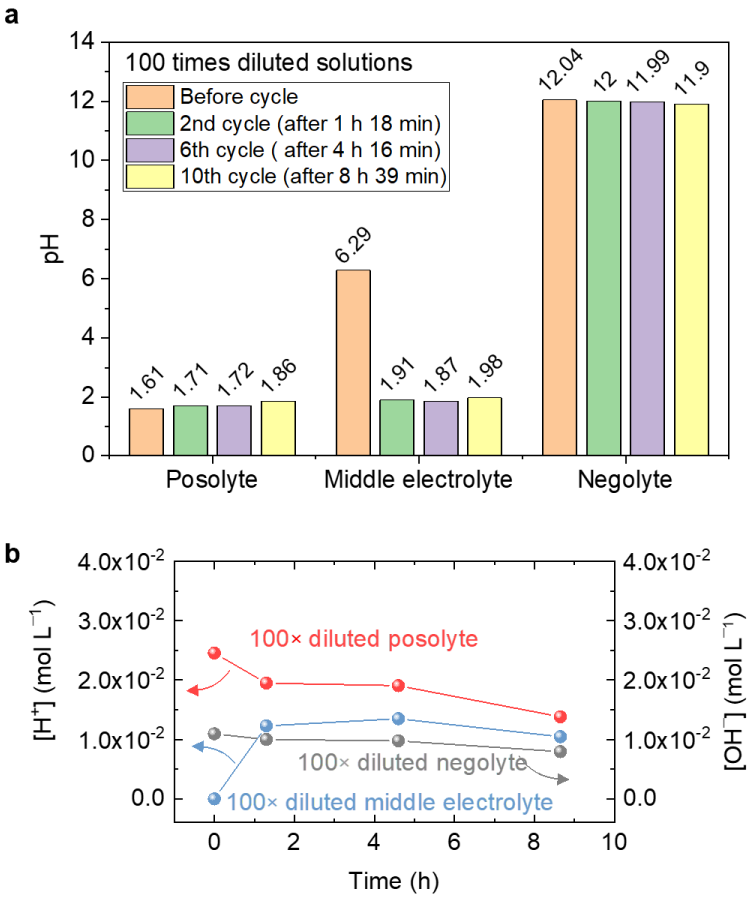

Figure S15. (a) pH measurement of 100× diluted solutions; 0.1 M FQH_2 posolyte, 3.0 M NaCl middle electrolyte and 0.2 M $[Zn(OH)_4]^{2-}$ negolyte during cycle tests. (b) The concentration change of protons and hydroxide a function of cycle time.

Calculation part

We note that, although the numerical values appearing in these calculations are particular to the cell whose performance is shown in Figure 2, the approach is generally applicable to all pH-differential cells.

2.1 Calculation of the leakage current density from the acidic posolyte

1) Number of protons leaking out of the posolyte during cycling
($\Delta C = [H^+]_{\text{after cycling}} - [H^+]_{\text{initial}} = 1.07$ M, posolyte volume : 7 mL)

$$= \frac{1.07 \text{ mol } H^+}{\text{L}} \times \frac{7 \text{ mL}}{10^3 \text{ mL/L}} \times \frac{6.02\times10^{23}}{\text{mol}} = 4.51 \times 10^{21} \text{ } H^+$$

2) Average proton flux from the posolyte during cycling (Cell area: 5 cm^2, cycling duration: 31,140 seconds)

$$= \frac{4.51\times10^{21} H^+}{5 \text{ cm}^2 \times 31{,}140 \text{ s}} = 2.90 \times 10^{16} \frac{H^+}{\text{cm}^2\cdot\text{s}}$$

3) Equivalent leakage current density from the crossover of protons during cycling

$$= \frac{2.90\times10^{6} H^+}{\text{cm}^2\cdot\text{s}} \times \frac{\text{mol}}{6.02\times10^{23}} \times \frac{96{,}485 \text{ C}}{\text{mol } H^+} = 4.64 \times 10^{-3} \text{ A cm}^{-2} = 4.64 \text{ mA cm}^{-2}$$

2.2 Calculation of the leakage current density from the basic negolyte

1) Number of hydroxide ions leaking out of the negolyte during cycling
($\Delta C = [OH^-]_{\text{after cycling}} - [OH^-]_{\text{initial}} = 0.3021$ M, negolyte volume: 10 mL)

$$= \frac{0.3021 \text{ mol } OH^-}{\text{L}} \times \frac{10 \text{ mL}}{10^3 \text{ mL/L}} \times \frac{6.02\times10^{23}}{\text{mol}} = 1.82 \times 10^{21} \text{ } OH^-$$

2) Average hydroxide flux from the negolyte during cycling (Cell area: 5 cm^2, cycling duration: 31,140 seconds)

$$= \frac{1.82\times10^{21} OH^-}{5 \text{ cm}^2 \times 31140 \text{ s}} = 1.17 \times 10^{16} \frac{OH^-}{\text{cm}^2\cdot\text{s}}$$

3) Equivalent leakage current density from the crossover of hydroxide ions during cycling

$$= \frac{1.17\times10^{16} OH^-}{\text{cm}^2\cdot\text{s}} \times \frac{\text{mol}}{6.02\times10^{23}} \times \frac{96{,}485 \text{ C}}{\text{mol } OH^-} = 1.87 \times 10^{-3} \text{ A cm}^{-2} = 1.87 \text{ mA cm}^{-2}$$

2.3 Thermodynamic minimum work for rebalancing by restoring H^+ and OH^-

1) Ideally, to take protons from a concentration of 10^{-7} M in water, and move them to the initial concentration of 2.5 M H^+ HSO_4^- in the posolyte,

$$\Delta G = \bar{R}T\ln\frac{2.5 \text{ M } H^+}{10^{-7}\text{M } H^+} = \frac{8.314 \text{ J}}{\text{mol}\cdot\text{K}} \times 298 \text{ K} \times \ln\frac{2.5 \text{ M}}{10^{-7}\text{M}} = 42.20 \text{ kJ mol}^{-1} \approx 0.44 \text{ eV},$$

where G is Gibbs free energy and $\bar{R}$ is the universal gas constant.

2) Ideally, to take hydroxide ions from a concentration of 10^{-7} M in water, and move them to the initial concentration of 3.6 M NaOH in the negolyte.

$$\Delta G = \bar{R}T\ln\frac{3.6 \text{ M } OH^-}{10^{-7}\text{M } OH^-} = \frac{8.314 \text{ J}}{\text{mol}\cdot\text{K}} \times 298 \text{ K} \times \ln\frac{3.6 \text{ M}}{10^{-7}\text{M}} = 43.11 \text{ kJ mol}^{-1} \approx 0.45 \text{ eV}.$$

3) For taking a proton-hydroxide pair from pH 7 water to the initial posolyte and negolyte pH,
Total amount of energy = $42.20 \text{ kJ mol}^{-1} + 43.11 \text{ kJ mol}^{-1} = 85.31 \text{ kJ mol}^{-1} = 0.88$ eV;
thus the required voltage for the rebalancing cell is V_{rebal} **= 0.88 V**.

4) Considerations regarding the practical operating voltage of an *n*-cell rebalancing stack:

Estimated voltage should depend upon current density, i, as follows:

$$= n\left[V_{rebal} + i\left\{\sum \rho_{sol}\, t_{sol} + \sum (r_{CEM} + r_{AEM} + r_{BPM})\right\}\right] + \eta_{HER}(i) + \eta_{OER}(i)$$

where the sum is taken over the components in a single repeating unit; ρ_{sol} is the solution resistivity; t_{sol} is the thickness of the solution in a single cell; r_{CEM} , r_{AEM}, and r_{BPM} represent the area-specific resistance of the cation exchange membrane, the anion exchange membrane, and the bipolar membrane respectively; $\eta_{HER}(i)$ is the overvoltage of the hydrogen evolution reaction on one end-plate of the stack, and $\eta_{OER}(i)$ is the overvoltage of the oxygen evolution reaction on the other end-plate of the stack. In employing a rebalancing stack instead of a single cell, the OER and HER overvoltages become spread thinly over an arbitrarily large number of cells.

2.4 Minimum power loss from the salt splitting process

1) Loss of total current during the cell cycling (Cell area: 5 cm^2) is determined by the majority crossover species. The salt splitting process will produce equal amounts of protons and hydroxide, with the pH leakage minority species used to both restore the initial pH and neutralize the middle electrolyte

1.1) Loss current of $H^+ = \frac{4.64\ \text{mA}}{\text{cm}^2} \times 5\ \text{cm}^2 = \mathbf{23.20\ mA}$ (majority)

1.2) Loss current of $OH^- = \frac{1.87\ \text{mA}}{\text{cm}^2} \times 5\ \text{cm}^2 = 9.36$ mA (minority)

1.3) Accumulation current of H^+ in the middle electrolyte = 23.20 mA (H^+) – 9.36 mA (OH^-) = 13.84 mA

1.4) At the ideal cell voltage of 0.88 V, the salt splitting process could restore protons to the posolyte, hydroxides to the negolyte and use the remaining hydroxides to neutralize the proton accumulation in the middle electrolyte; in this case,

Power loss = 0.88 V × 23.20 mA = **20.4 mW,**

Power consumed to rebalance pH leakage per unit area of membrane = $\frac{20.4\ \text{mW}}{5\ \text{cm}^2}$ = **4.08 mW cm^{-2}**.

2.5 Estimated system RTEE of cell augmented with pH restoring process

If we run the battery at a current density of 20 mA cm^{-2}, the discharge power density is 40 mW cm^{-2} from the power density curve reported in Figure S21. However, the energy put into charging the cell is delivered during only half of the duty cycle, whereas the power loss from pH leakage continues throughout the entire charge-discharge cycle. Thus, the pH restoration process consumes a minimum of $\frac{4.08\ \text{mW cm}^{-2}}{(40\ \text{mW cm}^{-2})/2} \approx$ **20.4%** of the energy put into charging. The round-trip EE of 71.8% (Figure 2b) implies that an additional 20.4% of the charging energy is lost in operating the hybrid RFB. Increasing the operating current density would decrease the fraction of the charging energy lost to pH restoration while increasing the fraction lost to internal impedance; this tradeoff would lead to an optimum current density for maximizing energy efficiency. We did not explore this optimization. Under the conditions explored, the round-trip energy efficiency of the hybrid RFB augmented with the pH restoring cell is estimated to be around 51%. This estimate is approximate not only because it is based on the thermodynamic minimum required voltage but also because it is based on the average pH leakage rate obtained from a single measurement after many charge-discharge cycles, whereas one would actually operate an augmented system in a way such that the pH leakage was offset before it led to large pH changes. Despite these uncertainties,

improvements in membrane permselectivity appear necessary in order to enable practical pH-differential cells to operate with high efficiency.

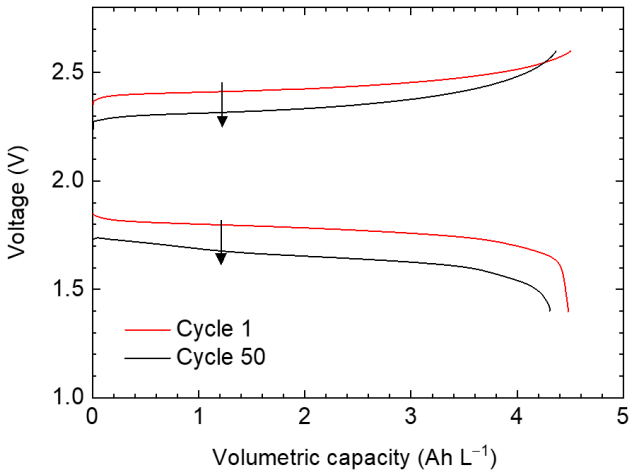

Figure S16. Voltage profile of 0.1 M FQH_2 posolyte at cycles 1 and 50 of the experiment reported in Figure 2a, showing the decreased charge and discharge voltages during cycling at 20 mA cm^{-2}. This is attributed to the change in pH of the posolyte and negolyte toward more neutral values, decreasing the OCV.

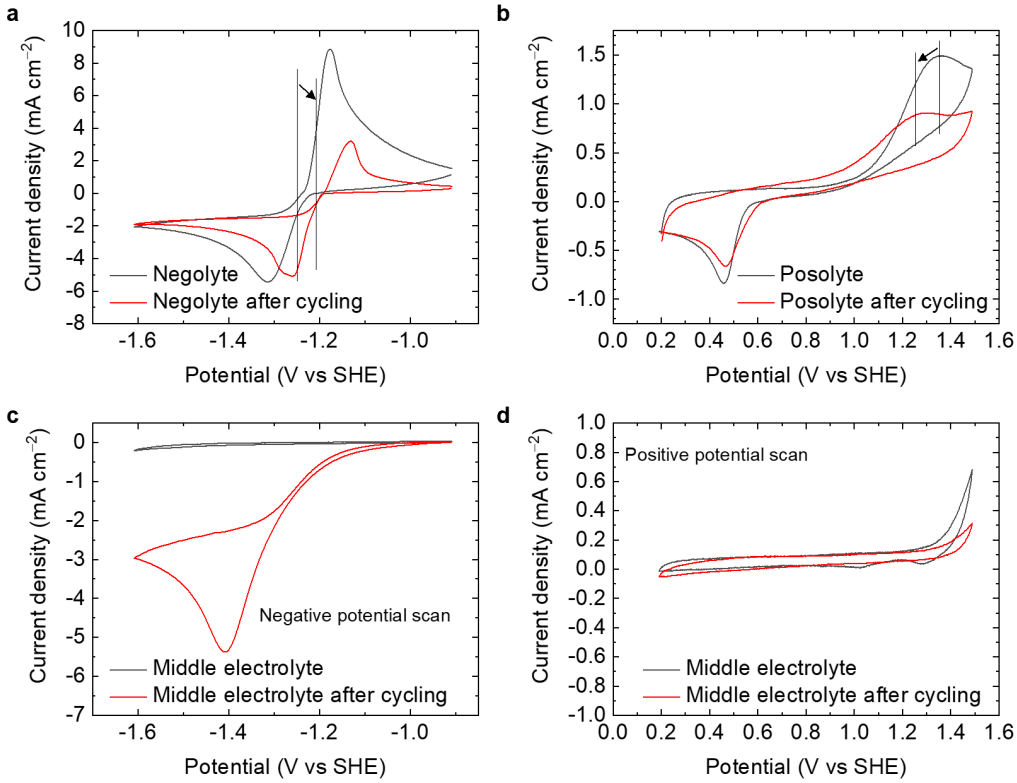

Figure S17. Cyclic voltammetry curves (CVs) of the (a) negolyte and (b) posolyte on the pristine glassy carbon electrodes before and after cycling reported in Figure 2a. CVs of the middle electrolyte on the pristine glassy carbon electrodes before and after cycling in the (c) negative (d) positive potential windows at a scan rate of 10 mV s^{-1}.

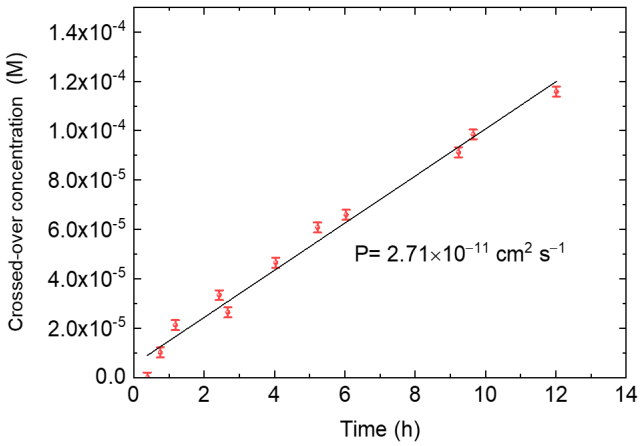

Figure S18. The permeability of FQH_2 across the DSV anion exchange membrane. The permeability is calculated from the rate of increase of the crossed-over FQH_2 concentration in the receiving reservoir.

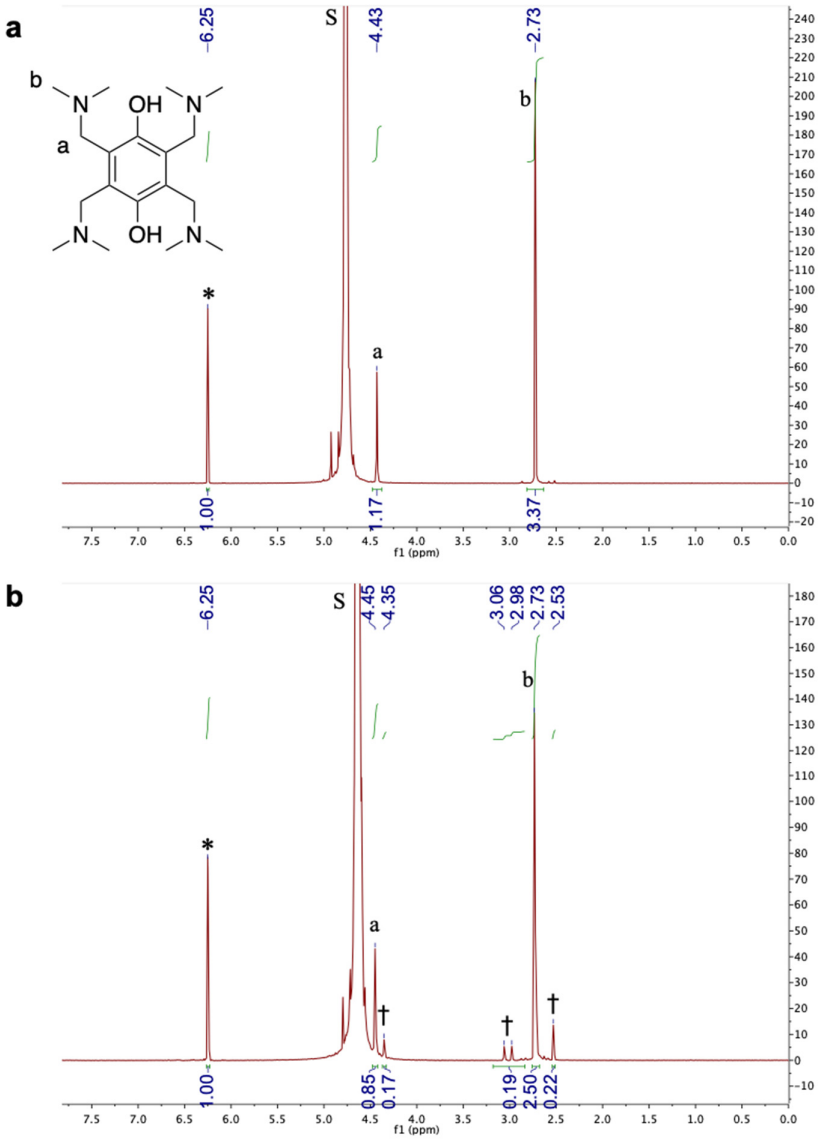

Figure S19. ^{1}H-NMR spectrum of the 0.1 M FQH_2 posolyte before and after 50 cycles of the experiment reported in Figure 2a. In both cases, 100 µl of electrolyte was diluted into 700 µl D_2O with 50 mM maleic acid standard. In the ^{1}H NMR spectrum of pristine FQH_2 in D_2O, S is the trace H_2O solvent peak, * is the peak from internal standard maleic acid. The peak at 4.43 ppm is the proton of $-CH_2-$ group, and the peak at 2.73 ppm is the proton of $-CH_3$ group. In general, the proton from –OH group is not observed due to the exchange with deuterium. In the ^{1}H NMR spectrum of cycled FQH_2 in D_2O, the new emerged small peaks at 4.35, 3.06, 2.98 and 2.53 ppm are from the unidentified decomposed compound. The new compound observed in the cycled electrolyte is similar in structure to the starting material.

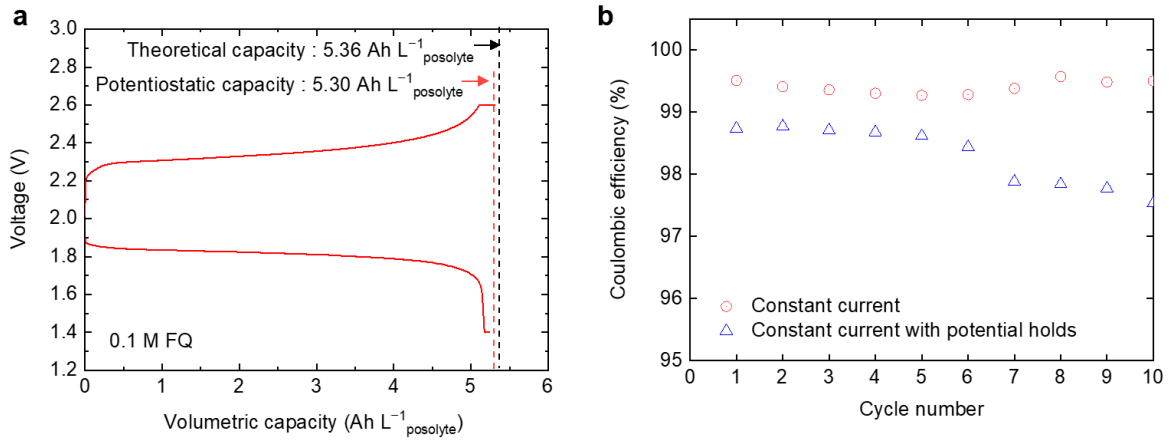

Figure S20. (a) Charge-discharge voltage profile of the 0.1 M FQH_2 posolyte at a current density of 20 mA cm^{-2} with cutoff voltages of 1.4 and 2.6 V with charge-discharge potential holds until the current density decreases to 1 mA cm^{-2}. The potentiostatic capacity was 98.8% of theoretical capacity. (b) Comparison of Coulombic efficiency of the different charge-discharge conditions; a constant current of 20 mA cm^{-2} with and without potential holds. The change at cycle 7 suggests that there might be a side reaction during the potential hold in the zinc-based flow cell.

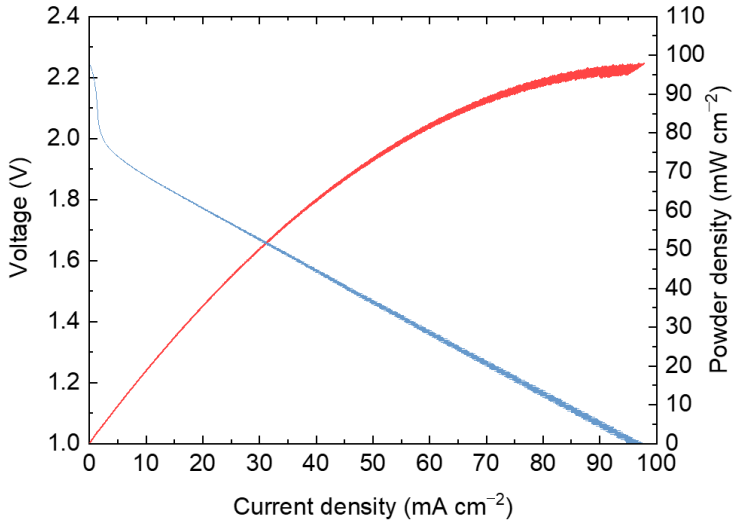

Figure S21. Cell voltage (blue) and power density curves (red) versus current density of 0.1 M FQH_2 posolyte from a fully charged state. A peak power density was 97.8 mW cm^{-2} at a current density of 96.8 mA cm^{-2}.

Table S1. Performance comparison of acid-alkaline hybrid batteries. "N.A.": not available

Hybrid cell (year)	**Type**	**Electrolyte compositions (Negolyte|middle electrolyte|posolyte)**	**Membrane (CEM/AEM)**	**Cell potential (V)**	**Current density (mA cm^{-2})**	**# of Cycles (hours)**
Zinc-FQH_2 **(This work)**	Flow cell	0.2 M $Na_2[Zn(OH)_4]$ in 3.6 M NaOH, 0.1 g Zn|3 M NaCl|0.1 M FQ in H_2SO_4	Nafion117 /Selemion DSV	2.0	15 – 40	50 (42)
Zinc-Vanadium **(This work)**	Flow cell	0.2 M $Na_2[Zn(OH)_4]$ in 3.6 M NaOH, 0.1 g Zn|3 M NaCl|0.1 M $VOSO_4$ in 2.5 M H_2SO_4	Nafion117 /Selemion DSV	2.3	15 – 40	100 (43)
Zinc-Hydroquinone (2018)[3]	Static cell	Zn plate + 0.5 M NaOH ||0.1 M HQ in 0.1 M H_2SO_4 + 0.1 M Na_2SO_4	Solid electrolyte (Nasicon, $Na_3Zr_2Si_2PO_{12}$)	1.6	0.5 – 2.0	100 (N.A.)
Zinc-Ferricyanide (2018)[4] (pH 7)	Flow cell	$ZnCl_2$ |NaCl|$K_3Fe(CN)_6$ + $K_4Fe(CN)_6$	Fumasep FKE-50 /ASTOM Neosepta AFX	1.25	0.7 -2.5	7 (N.A.)
Zinc-Iron (2015)[5]	Flow cell	0.3 M $Na_2[Zn(OH)_4]$ + 0.5 M NaCl in 2.4 M NaOH |3 M NaCl|0.6 M $FeCl_2$ + 0.5 M NaCl in 1 M HCl	Nafion117 /Fumasep FAA-3	1.99	50 – 150	20 (12)
Zinc-Cerium (2014)[6]	Flow cell	0.5 M $Na_2[Zn(OH)_4]$ in 3 M NaOH |4 M $NaClO_4$|0.5 M $Ce(ClO_4)_3$ in 2.5 M $HClO_4$	Nafion1135 /Fumasep FAA	3.1	5	6 (50)
Sulfur-Iron (2014)[6]	Flow cell	1 M Na_2S_4 in 1 M NaOH |3 M NaCl|1 M $FeCl_2$ in 1 M HCl	Nafion1135 /Fumasep FAA	1.22	5	6 (50)
Lead-Nickel metal hydride (2011)[7]	Static cell	$NiMH_x$ in 2 M KOH |0.2 M $K_2SO_4PbO_2$ in 1 M H_2SO_4	CMI-7000S /AMI-7001S	2.64	4.16	7 (40)

References

(1) Ryu, J.; Park, M.; Cho, J., Catalytic Effects of B/N-co-Doped Porous Carbon Incorporated with Ketjenblack Nanoparticles for All-Vanadium Redox Flow Batteries. *J. Electrochem. Soc.* **2016,** *163* (1), A5144-A5149.
(2) Goulet, M.-A.; Aziz, M. J., Flow Battery Molecular Reactant Stability Determined by Symmetric Cell Cycling Methods. *J. Electrochem. Soc.* **2018,** *165* (7), A1466-A1477.
(3) Yu, X.; Manthiram, A., Electrochemical Energy Storage with an Aqueous Zinc–Quinone Chemistry Enabled by a Mediator-Ion Solid Electrolyte. *ACS Appl. Energy Mater.* **2018,** *1* (2), 273-277.
(4) Desai, D.; Beh, E. S.; Sahu, S.; Vedharathinam, V.; van Overmeere, Q.; de Lannoy, C. F.; Jose, A. P.; Völkel, A. R.; Rivest, J. B., Electrochemical Desalination of Seawater and Hypersaline Brines with Coupled Electricity Storage. *ACS Energy Lett.* **2018,** *3* (2), 375-379.
(5) Gong, K.; Ma, X.; Conforti, K. M.; Kuttler, K. J.; Grunewald, J. B.; Yeager, K. L.; Bazant, M. Z.; Gu, S.; Yan, Y., A zinc-iron redox-flow battery under $100 per kW h of system capital cost. *Energy Environ. Sci.* **2015,** *8* (10), 2941-2945.
(6) Gu, S.; Gong, K.; Yan, E. Z.; Yan, Y., A multiple ion-exchange membrane design for redox flow batteries. *Energy Environ. Sci.* **2014,** *7* (9), 2986-2998.
(7) Li, H.; Weng, G.; Li, C. Y. V.; Chan, K.-Y., Three electrolyte high voltage acid–alkaline hybrid rechargeable battery. *Electrochim. Acta* **2011,** *56* (25), 9420-9425.